Title: A Test Platform of Back-Projection Imaging with Stochastic Waveform Generation

Authors: Lingsen Meng[1,+,*], Tong Zhou[2,+,*], Han Bao[1], Liuwei Xu[1], Jean-Paul Ampuero[3]

Affiliations:

[1]Department of Earth, Planetary and Space Sciences, University of California Los Angeles, Los Angeles, CA, USA.

[2]Aramco Beijing Research Center, Beijing, P.R. China.

[3]Université Côte d'Azur, IRD, CNRS, Observatoire de la Côte d'Azur, Geoazur, Valbonne, France.

[+]: These authors have equal contributions.

Corresponding authors: Lingsen Meng (lsmeng@g.ucla.edu), Tong Zhou (tongzhou.geo@outlook.com)

Key Points:

- Developed a stochastic generator for realistic seismic wave incoherency, improving understanding of earthquake source imaging analyses.
- Incoherent Green's functions crucially enhance back-projection imaging, resolving complex rupture details.
- This work enables evaluations of fidelity and artifacts in advancing seismic imaging techniques and accurate rupture speed assessments.

Abstract:

Back-projection (BP) is a cornerstone method for imaging earthquake ruptures, particularly effective at teleseismic distances for deciphering large earthquake kinematics. Its superior resolution is attributed to the ability to resolve high-frequency (>1 Hz) seismic signals, where waveforms immediately following the first coherent arrivals are composed of waves scattered by small-scale seismic velocity heterogeneities. This scattering leads to waveform incoherence between neighboring stations, a phenomenon not captured by synthetic tests of BP using Green's functions (GF) derived from oversimplified 1D or smooth 3D velocity models. Addressing this gap, we introduce a novel approach to generate synthetic Incoherent Green's Functions (IGF) that include scattered waves, accurately mimicking the observed inter-station waveform coherence decay spatially and temporally. Our methodology employs a waveform simulator that adheres to ray theory for the travel times of scattered waves, aggregating them as incident plane waves to simulate the high-frequency scattered wavefield across a seismic array. Contrary to conventional views that scattered waves degrade BP imaging quality by reducing array coherence, our synthetic tests reveal that IGFs are indispensable for accurately imaging extensive ruptures. Specifically, the rapid decay of IGF coherence prevents early rupture segments from overshadowing subsequent ones, a critical flaw when using coherent GFs. By leveraging IGFs, we delve into previously unexplored aspects of BP imaging's resolvability, sensitivity, fidelity, and uncertainty. Our investigation not only highlights and explains the commonly observed "tailing" and "shadowing" artefacts but also proposes a robust framework for identifying different rupture stages and quantifying their uncertainties, thereby significantly enhancing BP imaging accuracy.

Plain Language Summary

Earthquakes release energy that travels through the Earth as seismic waves. Back-projection (BP) was used to create images of these earthquakes from the waves recorded by seismometers around the world. This helps us understand how earthquakes happen, including which parts of the fault moved. Traditionally, BP has relied on simplified models that assume seismic waves travel in a straightforward manner. However, as waves move through the Earth, they encounter various materials that scatter them in different directions, much like light scatters when it hits a foggy window. This scattering makes the waves more complicated by the time they reach seismometers. In this study, by simulating a more realistic scenario where waves scatter, we can create better images of earthquakes. This is important because it allows us to see not just the initial break but also how the rupture evolves over time, without parts of it being hidden by the complexities of wave scattering. This leads to a clearer picture of the entire earthquake process. Additionally, our work shows a more accurate way to estimate the speed at which the earthquake propagates. Understanding these speeds is crucial for assessing the earthquake's impact and improving our preparedness for future seismic events.

1 Introduction

Back-projection (BP) imaging is a cornerstone technique for delineating the rupture kinematics of significant earthquakes (Mw ~ 6.5+), playing a pivotal role in enriching our grasp of rupture physics and enhancing seismic and tsunami hazard mitigation strategies (Bao et al., 2022; Meng et al., 2014; Xie & Meng, 2020). Distinguished by its ability to pinpoint sources of potent and coherent high-frequency (0.1 - 10 Hz) seismic radiation, BP leverages the coherent seismic phases captured by densely spaced, large-aperture teleseismic arrays, offering insights unattainable through conventional finite source inversions (Kiser & Ishii, 2017). This method stands out for its minimal reliance on preconceived notions regarding fault geometry and slip parameterization, thus unveiling intricate details and complexities in kinematic rupture processes often overlooked by traditional kinematic source inversions that typically depend on longer-period seismic data (10 - 40 s).

BP's utility is further exemplified by its success in uncovering phenomena such as multi-branch ruptures, the instantaneous dynamic triggering of local aftershocks, frequency-dependent ruptures in subduction zone megathrust earthquakes, and high-frequency bursts near large-slip areas or geometric barriers (Meng et al., 2011; Meng et al., 2012a; Fan & Shearer, 2016; Kiser & Ishii, 2011; Yao et al., 2013; Uchide et al., 2013; Vallée & Satriano, 2014; Okuwaki & Yagi, 2018). Notably, BP affords more direct estimations of rupture dimensions and velocities, treating high-frequency radiation sources as proxies for tracking the rupture fronts (Meng et al., 2018).

Despite these advancements, the resolution and fidelity of the BP method is not completely understood. Studies utilizing deterministic synthetic waveforms as Green's functions for BP imaging tests (Okuwaki et al., 2018; Yin & Denolle, 2019; Zeng et al., 2019; Li et al., 2022) reveal a significant limitation: the simplified Green's functions derived from overly smooth 1D or 3D velocity models fall short of capturing the full spectrum of waveform complexities, thus failing to accurately model the relationship between the imaged radiators and the actual kinematics of the ruptures, as well as the associated uncertainties and biases in BP imaging.

The efficacy of BP imaging in revealing the kinematics of earthquake ruptures is largely attributed to its adeptness at capturing coherent, high-frequency seismic signals. Traditional wisdom suggests that a high degree of waveform coherence is essential for generating a high-quality BP image, facilitating the clear resolution of rupture processes (Rost & Thomas,

2002). Commonly, the artifacts observed in BP images are thought to arise from the waveform intricacies inherent to Green's functions (GFs), notably the P coda waves, which are influenced by scattering across the heterogeneous fabric of the Earth's interior.

Interestingly, these waveform complexities—particularly the incoherent elements within the P-coda waves—unexpectedly contribute to the success of BP imaging. The presence of low coherence in the coda waves plays a crucial role, as it allows for the imaging of continuous ruptures by ensuring that the BP signal strength from early sub-sources diminishes swiftly over time. This dynamic prevents early rupture phases from overshadowing later ones, a stark contrast to scenarios dominated by coherent coda waves. This nuanced understanding underscores the significance of waveform complexities in refining BP imaging outcomes, highlighting the intricate interplay between signal coherence and the visualization of seismic events.

The complexity inherent in GFs, pivotal to BP imaging, stems from the medium's heterogeneities on both the station side (Figure 1a) and the source side (Figure 1b). On the station side, crustal scattering causes a decay in waveform coherence, observable in teleseismic array recordings as a function of both time and distance between stations. Conversely, source-side scattering is linked to waveform complexity due to fault-damage-zone reflection and diffraction, adding another layer of complications to seismic waveform analysis.

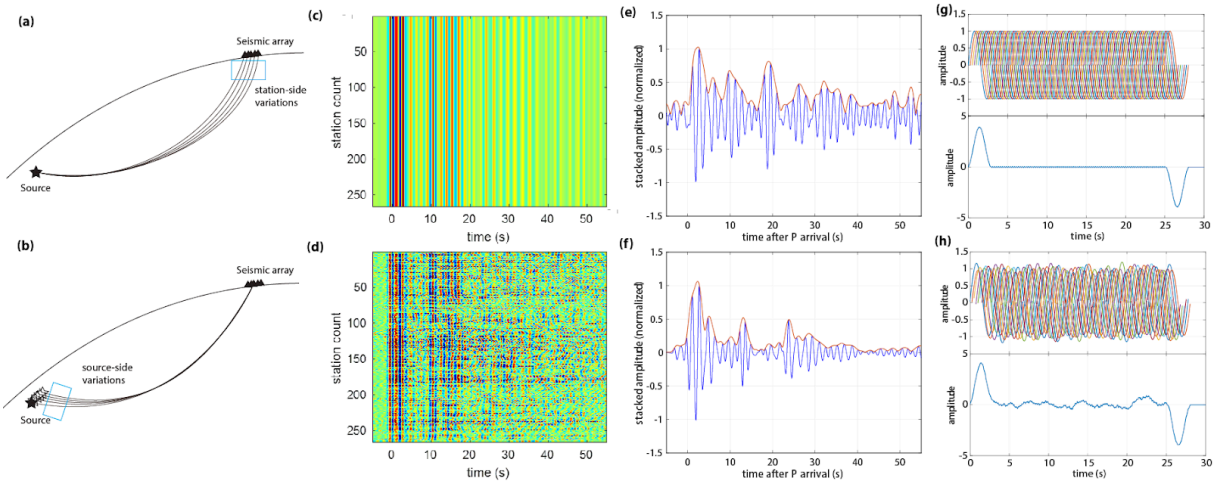

Figure 1. *Illustrative Overview of Green's Function Incoherency Origins. This figure captures the essence of incoherency within Green's functions, differentiating between station-side (a) and source-side (b) scattering and path variations. Panels (c) and (d) provide contrasts between a coherent Green's function, with amplitude represented through a colormap, and a more realistic depiction featuring incoherent components. Subsequent sections (e) and (f) detail the aggregated power from both coherent and incoherent Green's functions, respectively, with instances derived from the USArray's recordings during the 2020 Cayman Trough earthquake, situated in the Caribbean Sea Plate (refer to Figure 3a for context). Finally, diagrams (g) and (h) conceptualize the coherent Green's functions for individual sub-sources and the teleseismic recording of a homogeneous rupture at one station, alongside a representation of source-side incoherency within a homogeneous rupture's teleseismic recording, respectively.*

Green's functions generated by 1D velocity models show a lack of station-side incoherency (Figure 1c), which leads to a gradual decline in the stacked power of the P-coda waves (Figure 1e). This scenario can obscure the P-arrival from later sub-sources, effectively

"burying" them within the prominent P-coda waves emanating from preceding sub-sources. In contrast, more realistic Green's functions, characterized by station-side incoherency (Figure 1d), presents a coherent initial P arrival followed by subsequent incoherent coda waves. These incoherent coda waves do not constructively interfere, leading to a rapidly diminishing stacked power (Figure 1f). Such dynamics prevent an early sub-source from significantly overshadowing subsequent ones, facilitating a clearer delineation of the rupture sequence (see section 4.1 for more details).

Furthermore, source-side incoherency within Green's functions guarantees that teleseismic waveform recordings from each sub-source remain distinct, even if their source-time functions are identical. In cases of homogeneous (uniform slip and rise time) ruptures, Green's functions lacking source-side incoherency are prone to destructive interference among sub-sources (Figure 1g), which typically allows only the initial and final phases of the rupture to be captured by BP. The autonomy of each sub-source introduces variations in teleseismic recordings, disrupting the destructive interference pattern observed at teleseismic distances. This leads to waveform fluctuations that complement the initial and terminal phases (Figure 1h), thereby enabling the imaging of the entirety of the homogeneous ruptures (see section 4.2 for more details).

In this study, we begin by showcasing the coherence pattern within a teleseismic array, drawing upon empirical Green's Function (EGF) events from the 2020 Mw 7.7 Cayman Trough earthquake—one of the most significant strike-slip earthquakes in the Caribbean Sea (refer to Figure 3a). Subsequently, we introduce an innovative stochastic multi-plane-wave methodology for generating teleseismic Incoherent Green's Functions (IGF). This approach involves aggregating a series of incoming plane waves to closely match the observed coherence pattern of EGFs documented by a teleseismic array. Leveraging the IGFs produced through this novel technique, we undertake two important synthetic tests: one aimed at distinguishing between two seismic sources and another focusing on analyzing a homogeneous rupture. These exercises not only highlight the critical role of waveform incoherency but also serve to authenticate the IGFs' efficacy. Furthermore, they underscore the implications of incorporating IGFs into the arsenal of tools for future BP synthetic analyses, paving the way for more nuanced and comprehensive understandings of earthquake source imaging.

2 Quantifying Incoherence in Realistic Green's Functions

In this section, we quantify the incoherence in realistic GFs, which form the benchmark for our waveform modeling endeavors. To achieve this, we analyze the cross-correlation coefficient (cc) of seismic array recordings, specifically targeting the P wave train starting with the initial P arrival and spanning a 10-second window. To quantify waveform coherence, we employ a normalized cross-correlation coefficient cc within a chosen time window [t_s, t_e]:

$$cc(x_1, x_2) = \frac{\int_{t_s}^{t_e} u(x_1, t) \cdot u(x_2, t) dt}{\sqrt{\int_{t_s}^{t_e} [ux_1, t)]^2 dt \cdot \int_{t_s}^{t_e} [u(x_2, t)]^2 dt}} \quad (1)$$

Here, u(x) represents the velocity waveforms recorded by two distinct stations located at x_1 and x_2. Within the context of a seismic array, the coherence pattern CC is derived by calculating the average cc values across all pairs of stations within a specified inter-distance bin d.

$$CC(d) = \frac{\sum^{N} cc(x_1, x_2)}{N} \qquad if \quad d - \frac{\epsilon}{2} < |x_1 - x_2| < d + \frac{\epsilon}{2} \tag{2}$$

Where, Ɛ is the interval of the inter-distance bin d. Such a coherence pattern manifested across an entire array for a given earthquake event delineates the station-side incoherency. Drawing from our prior investigations into the coherence patterns of teleseismic P waves associated with global deep earthquakes (Zhou et al., 2022), a notable trend emerges: waveform coherence experiences a general decline as the interstation distance increases (Figure 2b). Additionally, the coherence pattern shows a decaying trend over time following the P wave's arrival (Figure 2a).

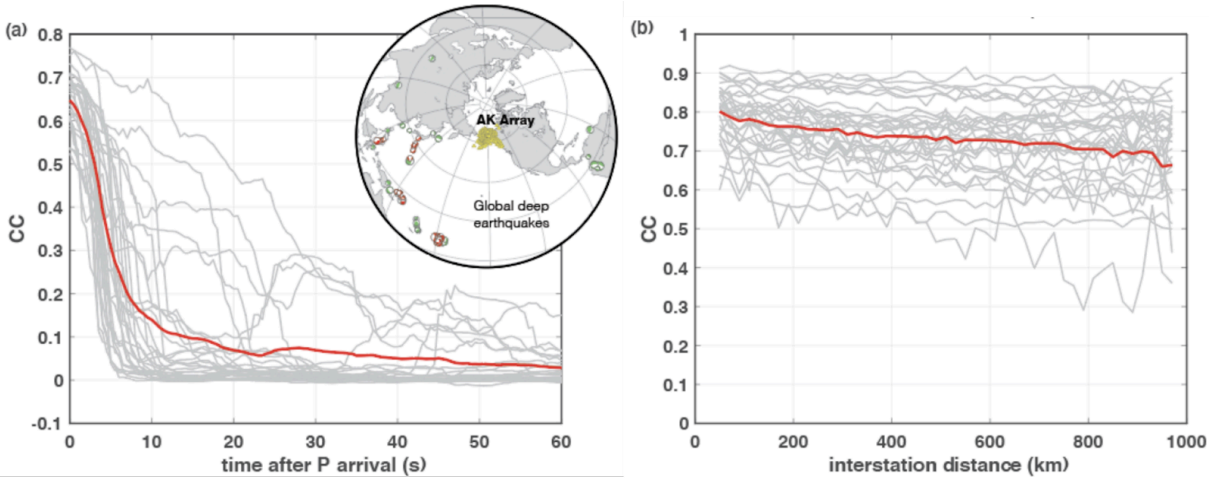

Figure 2. *Coherence Patterns of Global Deep Earthquakes Recorded by the USArray in Alaska. Panel (a) displays the coherence pattern, represented by the average cross-correlation (CC) values among station pairs within predetermined inter-distance bins, charted over time subsequent to the initial P-wave arrival. Individual earthquake measurements are denoted by gray curves, whereas the composite average across all events (color beach balls in the upper inset) is highlighted with the red curve. Panel (b) explores the CC values as a function of the distance between stations.*

To delve deeper into the coherence patterns of teleseismic waveforms, we focused on the source region of the 2020 Mw 7.7 Cayman Trough earthquake, as recorded by the USArray in Alaska (AK) (Figure 3a). The earthquake's hypocenter was located at 78.756°W, 19.419°N (NEIC). For our EGFs analysis, we selected three aftershocks within the fault zone, with magnitudes of M 5.4, M 5.1, and M 6.1, respectively (illustrated in Figures 3b-d). The waveforms from these EGFs, recorded by the Alaska array, were aligned based on the initial P arrival to ensure waveform coherence before being stacked together (Figure 3e), and were filtered within the 0.5-2 Hz frequency range.

Our analysis revealed distinct differences among the three EGFs. Specifically, EGF1 and EGF2 demonstrated similarities in their initial P arrivals and subsequent depth phases. The stacked waveforms (Figure 3e) highlighted that the peak amplitude of P-coda, approximately 10 seconds post-P arrival, carried roughly 50% of the direct P-wave's power across all three EGFs. However, EGF3, with a magnitude of M 6.1, presented more complex waveforms preceding the P-wave arrival, possibly indicating the coda wave of an earlier earthquake. Ideally, to accurately measure source-side incoherence and to potentially reconstruct a elongated rupture, a dense coverage of EGFs across the fault plane would be preferable.

Nevertheless, given the reality that only earthquakes with magnitudes above M5 are discernible with a decent signal-to-noise ratio (SNR) at teleseismic distances, available events are limited and sparsely distributed. In the context of the Cayman Trough earthquake sequence, this limitation meant that only three such earthquakes were available for analysis.

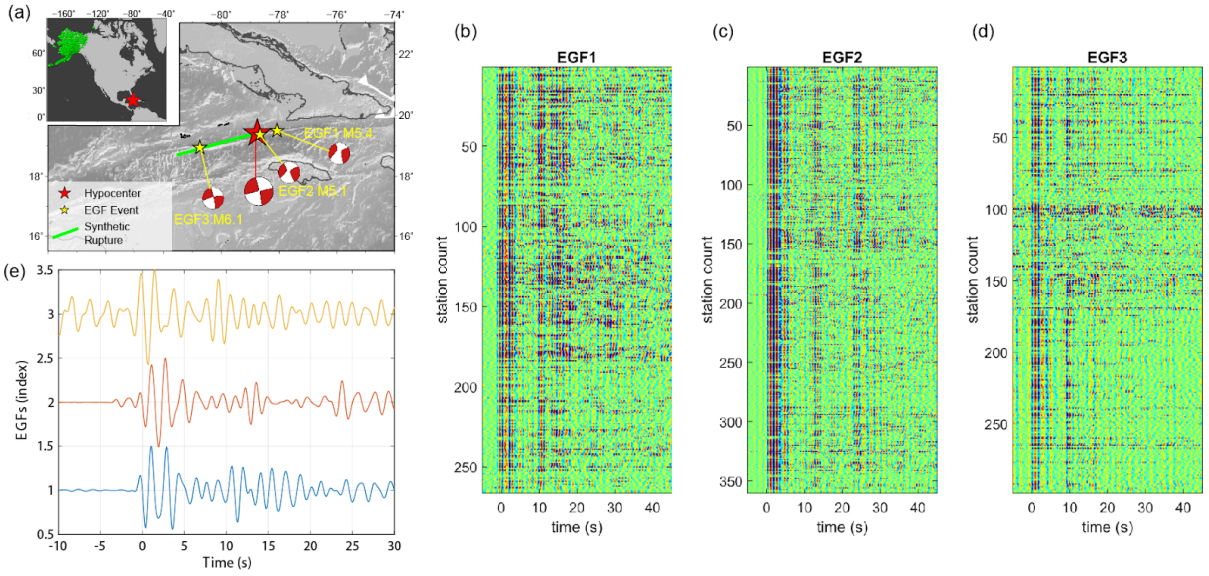

Figure 3. *Three EGFs in the Cayman Trough fault zone. (a) Tectonic settings. Outer panel shows the Cayman Trough fault plane (green line), mainshock (red star), and three aftershocks (yellow stars) with moment tensor solutions from global centroid moment tensor (gCMT) catalog. The fault plane is assumed to be along the strike direction of the mainshock. Inner panel shows the relative location of the fault zone (red star) and the USArray in Alaska (green triangles). (b-d) Aligned colormap showing the coherence of the three EGFs. Colormap represents the amplitude. (e) Stacked waveform (power) of the aligned waveforms of the three EGFs (normalized according to the maximum amplitude of each stacked EGF).*

Subsequently, we delve into the coherence patterns presented by each EGF, as illustrated in Figure 4. Within a specified narrow frequency band, we observe that the coherence pattern tends to decrease both over time and with increasing distance between stations, reflecting the influences of the station-side scatterings. To quantify the decay of coherence relative to the distance between stations, we adopt a consistent 10-second window commencing at the P-wave onset, calculating the cross-correlation (CC) for each pair of stations in the array. Distances between stations are categorized into 50 km bins, beginning from a minimum of 100 km, with the average CC value and its standard deviation documented for each bin (Figure 4a).

Additionally, the temporal decay of coherence, starting from the initial P-wave arrival, is evaluated using a moving window approach. This approach maintains a 10-second duration, advancing in 0.5-second increments. At every step, we compile and report the mean CC value across all station pairings (Figure 4b), offering insights into the temporal change of the seismic signal coherence.

Within a specified narrow frequency band (i.e., 0.5-2 Hz), we noted that the coherence patterns across the three EGFs displayed striking similarities (as shown in Figure 4c,d). Specifically, the CC values for EGF1 and EGF3 commence at approximately 0.77 at an interstation distance of 50 km, exhibiting an almost linear decline to values between 0.65 and 0.7 at distances extending to 2,500 km. In contrast, the CC value for EGF2 demonstrates a

more gradual decrease, from 0.92 at 50 km to 0.88 at 2,500 km. Regarding the temporal decay of CC values, all three EGFs start with high CC values (ranging from 0.78 to 0.88) at the onset of the first P arrival, which then precipitously fall to below 0.4 within 25 seconds post-P arrival.

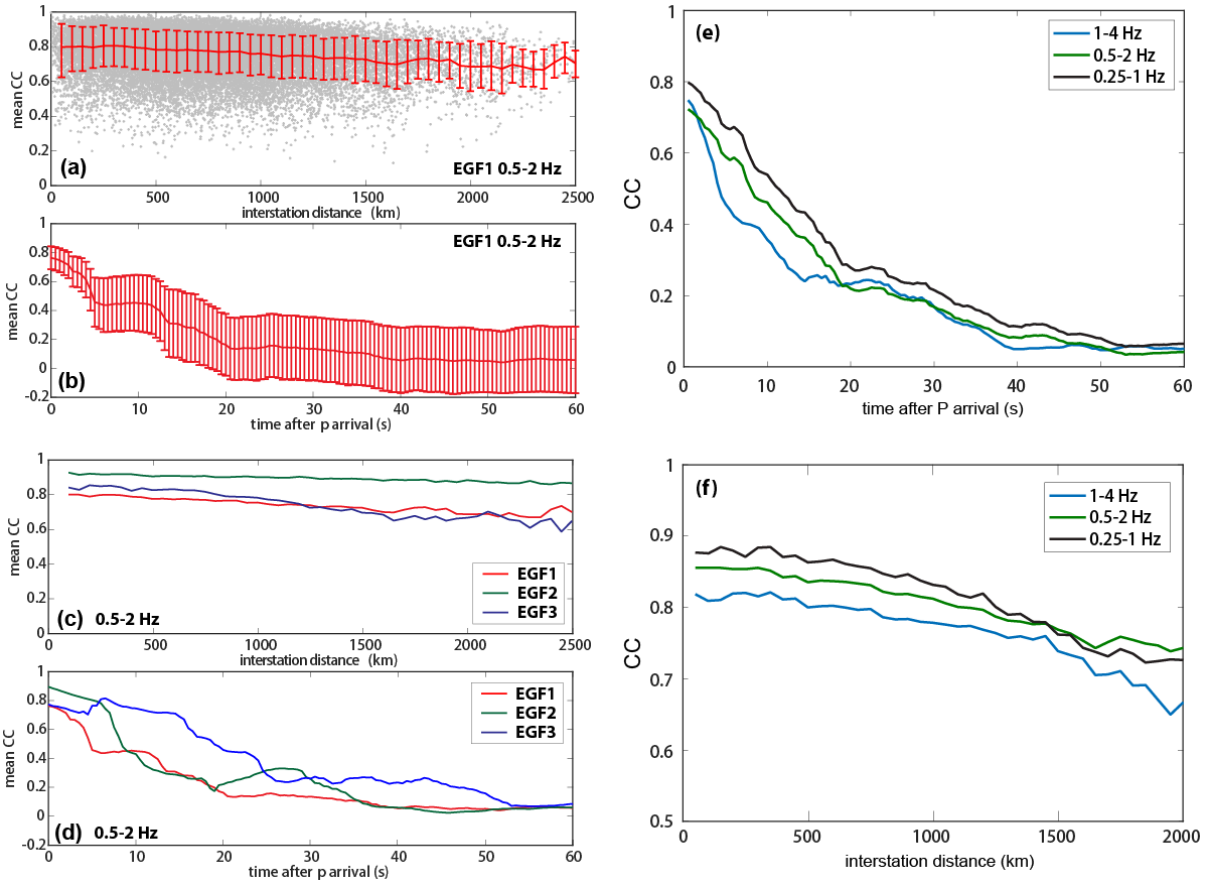

Figure 4. *Analyzing the Coherence Patterns of Empirical Green's Functions in the Cayman Trough Fault Zone. Panels (a) and (b) present the initial coherence measurements, employing the average cross-correlation coefficient (CC) across all station pairs, with error bars indicating the standard deviation of these CC values. These measurements, specifically for EGF1 within the 0.5-2 Hz frequency range, illustrate (a) the variation of CC relative to interstation distance and (b) the change in CC over time following the P-wave onset. Panels (c) and (d) extend this analysis to encompass the coherence patterns of all three EGFs within the same frequency band, examining (c) interstation distance effects and (d) temporal decay post-P arrival. Panels (e) and (f) synthesize these observations, showcasing the overall coherence patterns across the fault zone: (e) aggregates the time-dependent coherence patterns from the three EGFs across varying frequency bands, while (f) compiles the spatial coherence trends.*

Given the shared coherence pattern among the three EGFs, we averaged the coherence functions to encapsulate the overall coherence patterns from the fault zone to the seismic array (illustrated in Figure 4e,f). This averaged coherence, assessed across three frequency bands (0.25-1, 0.5-2, and 1-4 Hz), reveals a consistent trend of coherence fluctuation relative to both interstation distance and time elapsed since the P-wave arrival. The initial 20 seconds post-P arrival witnesses a rapid decay in averaged coherence values, plummeting from between 0.72-0.8 to 0.25-0.3. From 20 to 60 seconds, this decay rate moderates, culminating in exceedingly low CC values around 0.6 seconds. The analysis shows a uniform linear

decline in coherence across all three frequency bands concerning interstation distance: starting with CC values of 0.78-0.82 at 250 km and diminishing to 0.68-0.78 at 2,000 km. The decline rate remains consistent across frequencies, although coherence at zero distance decreases with increasing frequency—a phenomenon partly attributed to local site conditions, particularly shallow subsurface variations, leading to waveform similarities of less than 1 even at zero distance.

Assessing source-side coherence poses its challenges, notably due to the scarcity of teleseismic observations of requisite EGFs characterized by small earthquakes within a single fault zone sharing a similar focal mechanism but varying locations. Such data could ideally be sourced from earthquake swarms or zones with recurring seismic activity. Despite these limitations, near-fault observations offer valuable insights into source-side coherence patterns, supported by observed waveform spatial correlation lengths of ~ 20 km within the source region, as derived from phase coherence fluctuation measurements of the LASA and NORSAR arrays in the 0.5 - 0.8 Hz band (Capon & Berteussen, 1974; Berteussen et al., 1975). These insights allow us to approximate the source-side coherence pattern with a degree of informed speculation.

3. Multi-Plane-Wave Method for Generating Incoherent Green's Functions

This section introduces a novel waveform simulator that leverages the superposition of multiple plane waves to effectively model incoherent GFs. Given the crucial role of incoherence in both station-side and source-side phenomena for generating realistic and dependable BP synthetic tests, our method aims to accurately simulate the high-frequency waveform characteristics inherent to realistic seismic events.

Traditionally, capturing the full scope of a seismic rupture's complexity might involve collecting EGF events for each subfault within the rupture zone. Ideally, these EGF events would range between magnitudes 4.5 and 6.5, aligning with the point-source assumption and ensuring a high signal-to-noise ratio. However, the scarcity of EGF events that adequately span the entire source region presents a significant challenge. An alternative approach involves generating synthetic GFs (SGFs) through numerical waveform modeling, utilizing 3D velocity structures derived from tomographic imaging and hypothesized subduction geometries. Yet, these models often fall short, offering overly smoothed representations that fail to capture essential high-frequency waveform details. Attempts to introduce random heterogeneity into these models have been made (e.g., Emoto & Sato, 2018), but the computational demands of such detailed waveform simulations on a global scale—particularly at the necessary high frequencies (~2 Hz)—are prohibitively high, with a single SGF computation at an epicentral distance of 50 degrees potentially taking over 1,278 days on a desktop workstation (an Intel Xeon Gold 6132@2.4GHz CPU with 14 cores).

To address these challenges, we propose a highly efficient simulator capable of producing high-frequency incoherent GFs without necessitating deterministic waveform modeling. Crucially, this simulator is designed to align with the observed coherence patterns of actual GFs, thereby enhancing the utility of array-processing techniques.

The methodology centers on the initial plane wave, signifying the teleseismic P-wave arrival, followed by a series of plane waves simulating the P coda waves as observed in array recordings. These subsequent waves, emanating from random Rayleigh scatterers near the raypath, arrive from a variety of azimuths described by a Gaussian distribution.

$$\alpha = N(\alpha_0, \sigma_\alpha)$$
$$\sigma_\alpha = \frac{\alpha_{max}}{t_h} t \quad (t \le t_h) \qquad (3)$$
$$\sigma_\alpha = \alpha_{max} \quad (t > t_h)$$

The distribution's mean azimuth, α_0, correlates with the initial P-wave arrival direction, with its standard deviation, σ_α, increasing linearly over time (Figure 5a-c). This pattern continues until reaching a specified maximum value, α_{max}, beyond the initial arrival period (threshold time t_h), as depicted in Figure 5d. Such a distribution aims to replicate the broadening azimuthal range of scattered waves encountered at later times, thereby contributing to the observed decay in waveform coherence with increasing inter-station distance. The synthetic Green's function can be written as:

$$G_{nk}(r_{nk}, t) = E(t) \cdot \sum_{i=1}^{M} \frac{w}{t_i} cos(\alpha_i - \alpha_0) G_{n0}(t - t_i - (r_{nk} - r_0) p cos(\alpha_i - \theta_{k0})) \qquad (4)$$

In this model, G_{nk} represents the Green's function from the n-th point source to the k-th station, where r_{nk} is the epicentral distance. r_0 and p are the mean epicentral distance and ray parameters, respectively. We anticipate the arrival of M plane waves within our designated time frame. The amplitude of each arriving plane wave is modulated by the cosine of the azimuth angle difference (α_i–α_0), adhering to the Rayleigh scattering radiation pattern and assuming the scatterer's proximity to the direct ray path. The amplitude diminishes inversely with travel time (t_i), respecting the geometric spread of body waves, as depicted in Figure 5c. The constant parameter w influences the overall weighting. The initial plane wave, or the seed function G_{n0}, emanates from the n-th source towards a reference station, comprising a 0.5-second half-period of a 1-Hz sine wave to mimic the point source's initial response. This is succeeded by a 9.5-second random time series, embodying a series of half-sine waves with randomized arrival times, with its maximum amplitude set to 10% of the initial sine wave to illustrate source-side incoherence due to heterogeneous fault zone propagation.

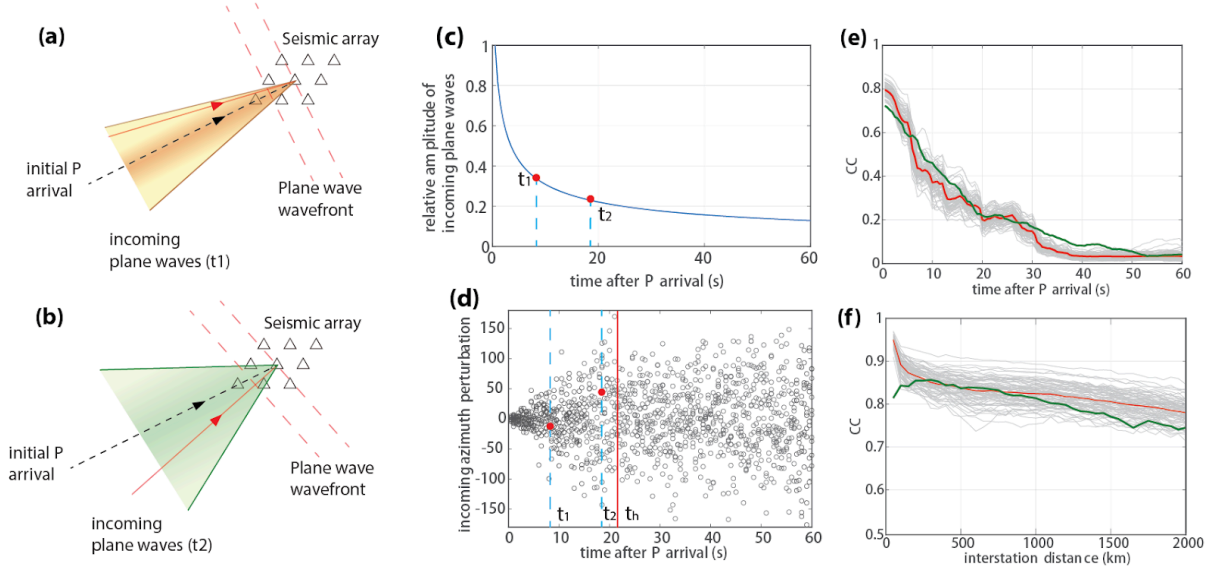

Figure 5. *Illustrating the Multi-Plane-Wave Method. Panels (a) and (b) depict incoming plane waves at two distinct travel times, t_1 and t_2, with their azimuths determined by a Gaussian distribution (highlighted area), represented by red dashed lines for clarity, and the*

direction of propagation indicated by solid red arrows. Panel (c) shows the amplitude decay factor relative to time post-P-wave arrival, with arrival times t_1 and t_2 highlighted for reference. Panel (d) presents a scatter plot illustrating the variability in incoming azimuths as a perturbation from the P-wave's azimuth over time; here, gray circles denote individual plane waves, while red dots highlight specific waves at t_1 and t_2, underscored by cyan dashed lines, with the threshold time demarcated by a red line. Panels (e) and (f) display the coherence patterns adjusted for time post-P-wave arrival and interstation distance, respectively. The gray curves map out the coherence pattern across 100 implementations of the IGF using the multi-plane-wave approach, with the red curve summarizing the average coherence pattern from these implementations. The green curve reflects the coherence pattern derived from empirical Green's Functions, with all patterns assessed within the 0.5-2 Hz frequency band.

Given the absence of direct measurements for short-wavelength heterogeneity within the fault zone, seed functions are produced with a 20 km spatial correlation length in the source region, inspired by the P-wave phase coherence fluctuation analysis from the LASA and NORSAR array within the 0.5 - 0.8 Hz band (Capon & Berteussen, 1974; Berteussen et al., 1975). The shared path and receiver effects across different fault patches necessitate a uniform azimuth variable α_i for all sources. The factor $E(t)$ adjusts the envelope of the synthetic incoherent Green's function, with the envelope of stacked empirical Green's functions providing a basis to preserve relative amplitude details post-first P phase. Although ideally measured at each station, the low signal-to-noise ratio of EGFs at certain stations complicates direct envelope measurements. Hence, an averaged envelope suffices for relative amplitude comparisons in BP analysis.

Equation (3) outlines three pivotal parameters—maximum azimuth range ($\alpha_{\max}$), threshold time (t_h), and plane wave density (M)—identified through a grid-search method to align with the observed coherence decay over time and distance, based on empirical data in a least-square sense.

$$(\alpha_{max}, t_h, M) = \text{argmin}\{|\text{CC}_{\text{obs}}^{\text{time}} - \text{CC}_{\text{syn}}^{\text{time}}|^2 + |\text{CC}_{\text{obs}}^{\text{dist}} - \text{CC}_{\text{syn}}^{\text{dist}}|^2\} \quad (5)$$

This process, exemplified by the Cayman Trough earthquake analysis, successfully replicates the spatial and temporal coherence pattern with $\alpha_{\max}$=120°, t_m=18 seconds, and M=30 for the 0.5 - 2 Hz frequency band (Figures 5e-f). These empirically derived parameters, while effective for replicating observed coherence patterns, are not directly linked to the underlying scattering processes, which remains beyond this study's scope. Notably, waveform analysis within this frequency range illustrates pronounced incoherent components (Figure 6a) in stark contrast to the overly coherent 1D synthetic Green's functions (SGFs) (Figure 6b). The envelope of the IGF closely mirrors that of the EGFs, marking a significant advancement in our method's ability to efficiently simulate realistic incoherent GFs, thereby enhancing the fidelity of BP synthetic tests.

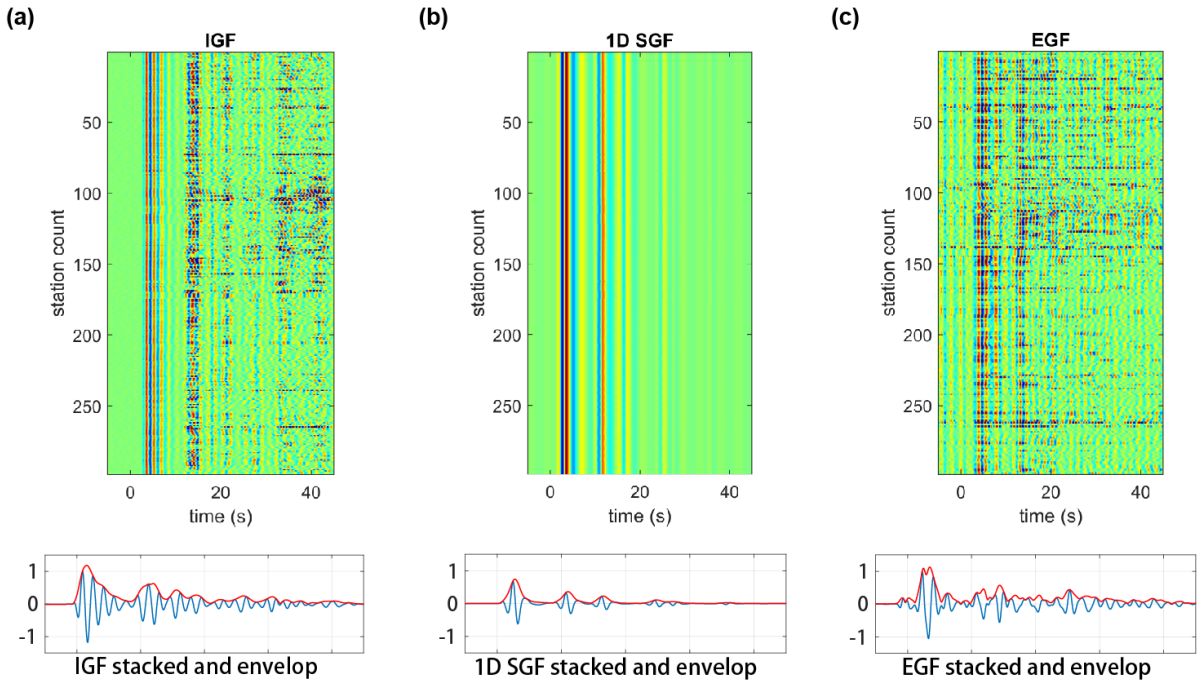

Figure 6. *Comparison of Waveforms and Their Stacked Envelopes. Panel (a) showcases the Incoherent Green's Functions (IGF) waveforms, panel (b) displays the 1-Dimensional Synthetic Green's Functions (1D SGF), and panel (c) illustrates the Empirical Green's Functions (EGF) waveforms. In each panel, variations in waveform amplitude are indicated by the color spectrum.*

4 Synthetic BP tests with incoherent GFs

In this section, we conduct two synthetic BP tests using IGFs to demonstrate the significance of incoherency of Green's functions to BPs. The first test is the BP of two competing sub-sources which shows the importance of coherence decay with time. The second test is the BP of a homogeneous rupture to show the ability that incoherency enables the imaging of the middle part of the homogeneous rupture. In general, we observe that our multi-plane-wave method generated IGFs consist of realistic high-frequency incoherent waves, which allows the BP to resolve the entirety of the homogenous rupture and is thus suitable for further BP synthetic tests.

4.1 Two competing sources

In this synthetic test, we simulate the source region of the 2020 Cayman Trough earthquake (as depicted in Figure 3a) with the USArray in Alaska serving as the seismic array. Two competing point sources are introduced: the primary source is located at the Cayman Trough earthquake's hypocenter (78.756°W, 19.419°N, NEIC), and the secondary 'competing' source is positioned 30 km west, with a 10-second delay, simulating westward rupture propagation at 3 km/s. This setup particularly aims to explore the interaction between the P-codas from the initial source and the direct P-wave from the subsequent source in BP imaging, assigning double the power to the first source compared to the second. To assess the impact of different Green's functions, we utilize synthetic GFs calculated with the 1D PREM earth model (1D SGF), the waveforms from an M5.4 aftershock as the EGF, and the IGF produced by our multi-plane-wave method.

The peak amplitude of the P-coda from the first source coincides with the direct P-wave from

the second source, both arriving with similar amplitudes and thus competing within the BP imaging framework. Figures 7a-c present the BP results from the competing-source tests using 1D SGFs, EGFs, and IGFs, respectively. The 1D SGFs fail to account for coherence decay over time or across station distances, whereas the EGFs, with their inherent incoherent components, allow for the resolution of the second source with less than 7 km of uncertainty (Figure 7b). The 1D SGF BP results exhibit a pronounced systematic location bias (over 15 km) favoring the first source (Figure 7a) and fail to identify any signals at the second source's location. In contrast, the IGFs successfully delineate the second source, albeit with some artifacts between the two sources (Figure 7c). This experiment demonstrates that when two signals of comparable power intersect, the coda waves from 1D SGFs can obscure or distort subsequent arrivals. It further illustrates the importance of realistically modeling GF coherence decay over time to prevent early subsources from overshadowing later ruptures. IGFs accurately mimic the decay of realistic GFs' coherency, significantly improving the resolution of competing sources.

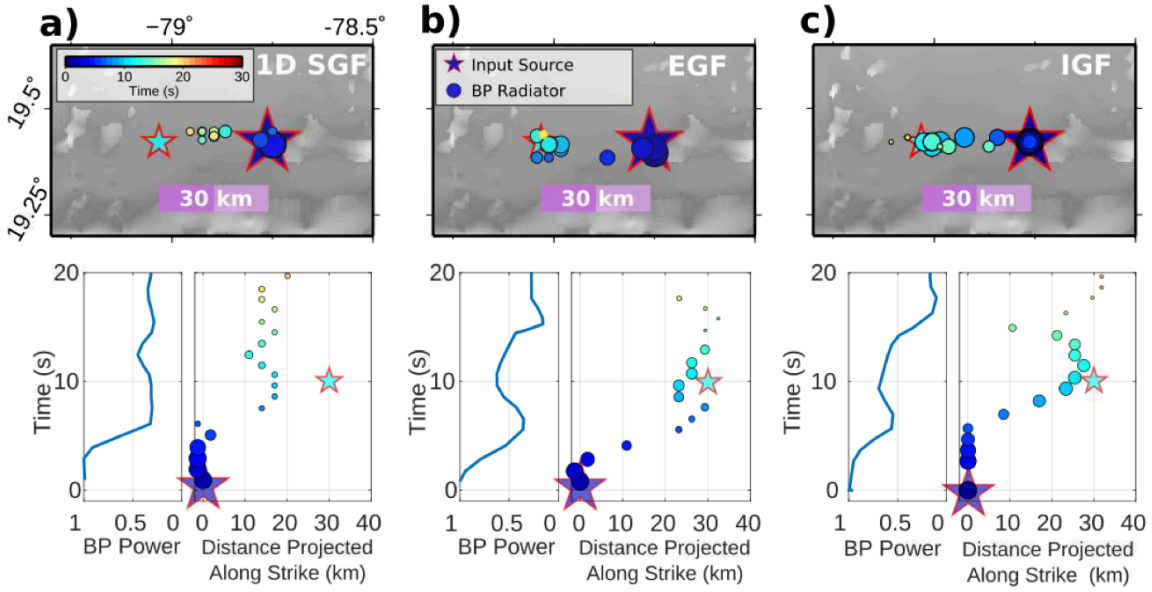

Figure 7. *Experiment of two competing sources. (a) (b) and (c) are BP results of the two competing sources when 1D synthetic GF (1D SGF), Empirical GF (EGF), and incoherent GF (IGF) are applied, respectively. Stars with red edges are the two input sources, and circles are the location of peak source radiation identified by BP. All symbols are color coded by time and scaled by relative powers.*

4.2 Analysis of a Homogeneous Rupture

Exploring the impacts of incoherent Green's Functions (GFs) originating from the source side provides valuable insights, particularly in the context of a homogenous rupture model. Here "homogeneous ruptures" refer to those with uniform source characteristic across the rupture zone (slip, shape of source time function, rise time, etc). In reality, ruptures are rarely homogenous but can be highly smooth especially on mature strike-slip faults and shallow portions of the megathrust faults (Meng et al., 2011). Figure 8 conceptualizes the challenges presented by perfectly coherent GFs within such a model, where each sinusoidal wave packet—emitted by individual sub-sources within a narrow frequency band—generates identical signals. This uniformity leads to destructive interference across the rupture's center, notably diminishing the presence of high-frequency signals and leaving only the starting/stopping phases to be imaged by BP.

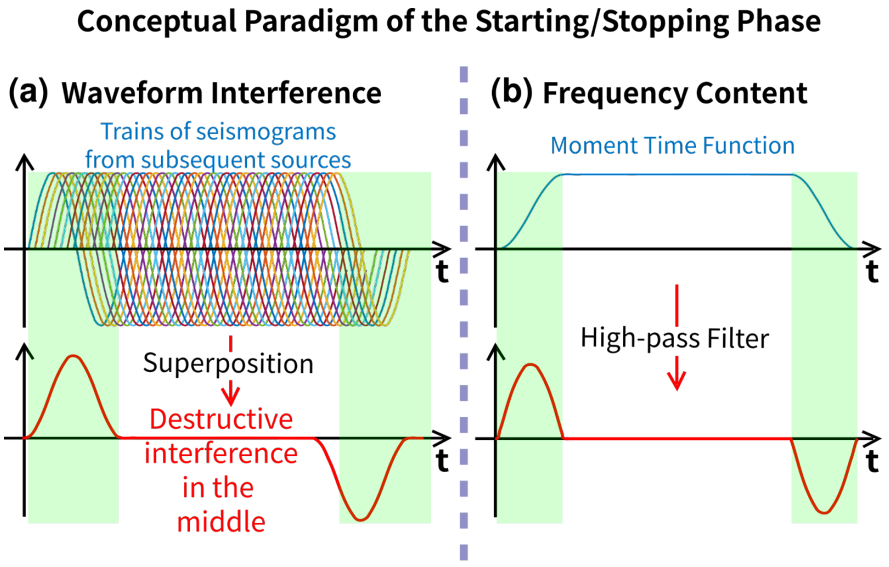

Figure 8. *Conceptual paradigms of destructive interferences in a homogenous rupture with perfectly coherent GFs, which explains the physical origins of starting/stopping phases. We present two different perspectives: (a) seismograms originated from different subsequent sources result constructively interfere in the beginning and the end but destructively interfere in the middle; (b) a high-pass filter applied over the moment-time function shows that in such settings, high-frequency signals are not correlated to the absolute moment rate but rather to the its fluctuations.*

To examine these effects, we conducted BP tests on a homogenous rupture model employing three distinct types of GFs: 1D synthetic GFs (Figure 9a), uniform EGFs based on M5.4 aftershock waveforms applied uniformly across all sub-sources (Figure 9b), and IGFs imbued with spatial variability for each sub-source (Figure 9c). These IGFs were generated using the multi-plane-wave method, ensuring significant wave incoherence both at the source and receiver ends.

Mirroring the conceptual demonstration, the BP analysis using uniform EGFs primarily highlights the rupture's initiation and termination phases (Figure 9b). However, spatial variability in GFs on the source side disrupts the pattern of destructive interference, facilitating the generation of high-frequency signals throughout the rupture. This effect is vividly captured in the BP test employing IGFs, which successfully delineates the propagating fronts across the entire rupture event (Figure 9c). Beyond the inherent incoherency in GFs, sudden variations in fault kinematics—such as changes in rupture speed, slip velocity, and the spatial arrangement of slip vectors across sub-fault patches—can similarly counteract destructive interference, producing pronounced signals within BP imagery (Li et al., 2020). Nonetheless, the application of incoherent IGFs enables BP to consistently resolve the movement of rupture fronts, even under conditions of gradual kinematic variation. This finding elucidates why BP analyzes often successfully depict the full extent of rupture propagation in numerous case studies.

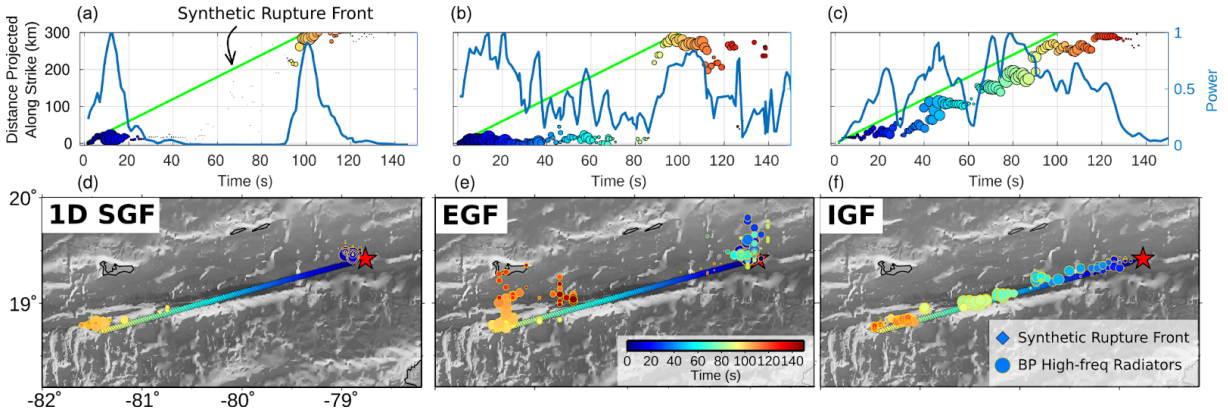

Figure 9. *Back-Projection Analysis of a Homogeneous Rupture Scenario. Panels (a) and (d) showcase BP images and their corresponding power levels derived from synthetic Green's Functions (GFs) based on a 1D seismic model (1D SGF). Panels (b) and (e) display results using a uniform empirical Green's Function (EGF), while panels (c) and (f) present outcomes from incoherent synthetic Green's Functions (IGFs). In this synthetic experiment, the input fault rupture (straight color line) is configured to span 300 km in length and 15 km in width, featuring a consistent slip of 5 meters. The rupture is designed to advance unilaterally westward at a velocity of 5 km/s, within the source region of the Cayman Trough earthquake, as illustrated in Figure 3a.*

4.3 Evaluating Tailing and Shadowing Artifacts in BP Imaging

Utilizing IGFs allows for the simulation of realistic incoherency, presenting a distinctive avenue to scrutinize artifacts within BP imaging that closely mirror actual conditions. This section investigates two commonly encountered artifacts in BP imaging: tailing and shadowing. Shadowing artifacts predominantly emerge at points of abrupt changes in rupture velocity, where bursts of high-frequency energy create local maxima in BP power, leading to the visualization of complex BP radiators. These artifacts, indicative of an apparent stagnation, often overshadow subsequent sources. This effect is visible as clustered radiators at the juncture of velocity change, coupled with a discernible gap at the onset of another rupture segment exhibiting a different speed (highlighted by a purple circle in Figure 10a). Conversely, tailing artifacts manifest as an extension of BP radiators beyond the actual cessation of rupture (illustrated by a pink circle in Figure 10a), attributed similarly to sudden alterations in rupture velocity at its termination.

When focusing solely on leading BP radiators, a gap becomes evident at points where the rupture velocity abruptly shifts or at the initiation/termination of a rupture segment (depicted in Figures 10b and 10d). Notably, both real observational BP results and synthetic BP analyzes employing IGFs exhibit these artifacts, as marked in Figures 10a and 10c. Thus, accurately identifying shadowing and tailing artifacts is crucial for the precise evaluation of rupture kinematics—such as determining the exact cessation of rupture, pinpointing changes between different rupture velocity regimes, and identifying segments likely to be misinterpreted due to artifact presence. Furthermore, the parallelism between artifacts generated by IGFs and those observed with EGFs (Figures 10a and 10c) underscores the efficacy of IGFs in producing BP images that reflect realistic scenarios, thereby enhancing our capability to assess and interpret these artifacts accurately.

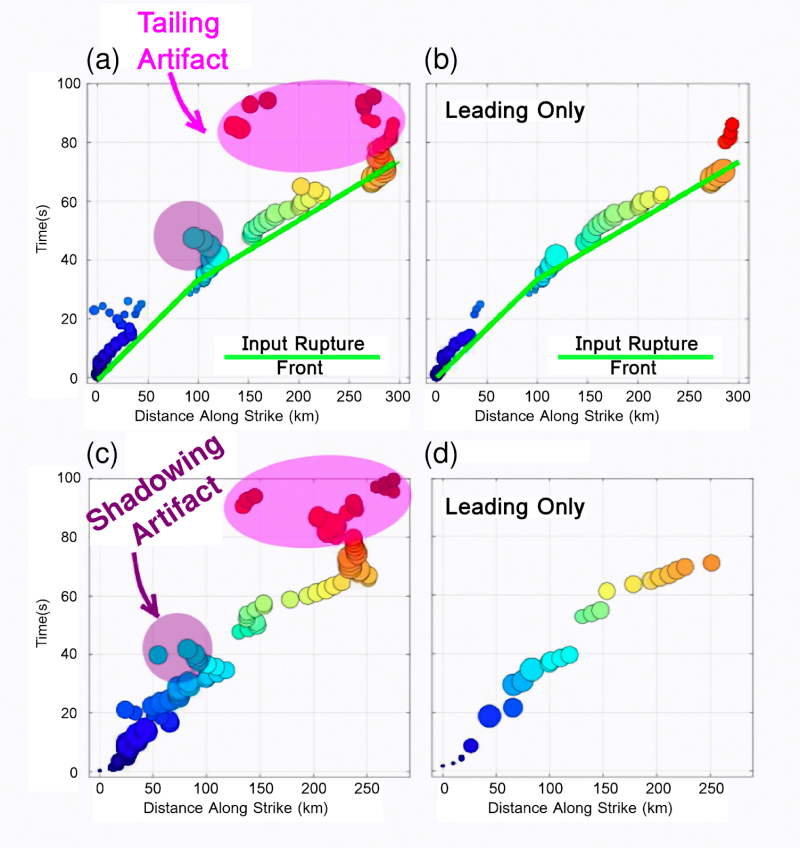

Figure 10. *Identifying Shadowing and Tailing Artifacts in BP Imaging of synthetic rupture scenarios with uniform slip and abrupt rupture speed change. The setting is to image the 2020 Mw 7.7 Cayman Trough Earthquake using the Alaska array (referenced in Figure 3a), this figure showcases BP imaging results. It plots the along-strike distances from the hypocenter against rupture times relative to the earthquake's origin time. Panel (a) demonstrates BP imaging with an EGF; Panel (b) isolates leading BP radiators for analysis; Panel (c) displays BP imaging using an IGF; and Panel (d) similarly focuses on leading BP radiators. Notably, the rupture velocities, inferred from the slope of the high-frequency (HF) radiators, exhibit variations between the intervals of 0-30 seconds and 50-70 seconds. The phenomena of "shadowing artifact" and "tailing artifact" are emphasized with purple and pink circles, respectively, while the green lines represent the input rupture fronts.*

5 Discussion

The multi-plane-wave method stands out for its efficiency in generating stochastic, high-frequency P-coda waves that align with realistic coherence decay patterns. While not deterministic—meaning it does not replicate the exact waveform details (wiggle by wiggle) of scattered waves—this method is particularly well-suited for array processing and BP analysis due to its accurate modeling of coherence decay. Leveraging the IGFs it produces, this technique enables the creation of a comprehensive test database aimed at addressing critical questions about BP imaging's resolution, sensitivity, fidelity, and uncertainty. Future work within this scope include assessing the reliability of BP-derived rupture speed estimates, particularly in the context of supershear earthquakes; understanding the extent to which BP's geometric complexities should be interpreted; exploring the relationship between BP power and kinematic source parameters; and evaluating novel earthquake source imaging methodologies and data sources, such as Distributed Acoustic Sensing (DAS) and smartphone-based detections.

Rupture speed, a crucial aspect of seismic source characterization, plays a significant role in ground shaking intensity and seismic hazard assessments. Directly tracing the rupture front movement via BP offers a straightforward approach to estimating rupture speed, yet a comprehensive analysis of associated uncertainties remains outstanding. Utilizing realistic IGFs facilitates systematic uncertainty assessments across various scenarios, from simple unilateral ruptures with constant speeds to more complex fault models featuring both uniform and non-uniform slip distributions derived from historical earthquakes. The insights garnered from this approach, which will be detailed in forthcoming publications, promise to enhance our understanding of supershear phenomena detection and offer valuable guidelines for interpreting BP-observed rupture speeds, especially in elongated ruptures (Bao et al., 2022). Further exploration will also delve into how depth phase contamination, abrupt changes in rupture speed, and bilateral ruptures may affect accurate rupture velocity measurements, providing a more nuanced understanding of the factors influencing BP analysis outcomes.

BP imaging has proven effective resolving a range of rupture dynamics, such as reverse rupture propagation (Hicks et al., 2020), bilateral ruptures (Xie et al., 2021), encirclement of rupture fronts (Meng et al., 2018), and fault jumps and steps (Meng et al., 2012a; Xie et al., 2021). The reliability of these complex observations underpins the confidence in their interpretation. Observations deemed trustworthy should inspire subsequent dynamic simulation studies, whereas findings of marginal confidence warrant cautious consideration. Employing IGFs for synthetic tests of various rupture scenarios, with attention to realistic path effects, enhances our ability to distinguish between genuine rupture radiators and artifacts in BP images—a crucial step in assessing the confidence level of BP analyses. Additional tests, incorporating complexities from dynamic rupture simulations, will explore their resolvability through BP, further refining our understanding of rupture mechanics.

The relationship between high-frequency seismic radiation (BP power) and specific source parameters remains indistinct, with differing interpretations such as direct slip acceleration (suggested by Fukahata et al., 2014 when GFs approximate a delta function) and scaling by the amplitude of depth-dependent GFs (Okuwaki et al., 2019). Prior studies lacking BP analysis with realistic incoherent GFs have not fully accounted for path effect influences, highlighting the need for re-evaluation using IGFs. Realistic IGFs also facilitate probing the kinematic source parameters that govern the high-frequency energies detected by BP, including slip, slip-rate, and the form of slip-rate functions. Moreover, exploring the source dynamics behind high-frequency energy generation—attributed to phenomena like barrier and asperity failures, heterogeneity in the brittle-ductile transition zone (Lay et al., 2012), fault roughness (Bruhat et al., 2016), and rapid healing in damage zones (Huang et al., 2016)—can provide deeper insights into earthquake rupture physics.

Beyond BP, various emerging array processing techniques aim to enhance the quality and robustness of source imaging. These include compressive sensing (Yao et al., 2011), MUSIC BP (Meng et al., 2012b), N-th root stacking (Fan & Shearer, 2015), Hybrid BP (Yagi et al., 2012), correlation-stacking (Fletcher et al., 2006), and BP with genetic-algorithm-based station selection (Kehoe & Kiser 2018). While efforts to test these methods against synthetic rupture scenarios have been made—for instance, investigations by Yin and Yao (2016) and Meng et al. (2012b) on the recovery of closely spaced simultaneous sources using 1D SGF—it's essential to reassess the efficacy of various BP techniques in different synthetic rupture scenarios, especially in the context of waveform complexities introduced by IGFs.

Emerging technologies like DAS and rotational seismology are drawing increased interest within the seismic research community. DAS systems, known for their capability to measure strain rate using densely spaced channels, offer unique advantages that may enhance the

resolution of source imaging and improve earthquake early warning systems near active faults (Li et al., 2023). A study by van den Ende and Ampuero (2021) highlighted that beamforming with DAS recordings is significantly influenced by scattered waves and local heterogeneities, rendering DAS channel recordings markedly less coherent than those from collocated nodal seismometers. This disparity could be attributed to DAS's directional sensitivity, velocity-enhanced damping, and the inherently incoherent nature of strain-rate measurements compared to velocity measurements. Synthetic tests using IGFs capturing such waveform complexity in DAS measurements will be crucial to understand its feasibility and uncertainty in seismic array processing.

Furthermore, the construction of synthetic test rupture scenarios has paved the way for developing machine learning models dedicated to identifying artifacts in BP imaging. Initially, artifacts and reliable BP radiators will be manually labeled in a vast array of synthetic BP tests based on our models. Subsequently, a Deep Learning (DL) model, such as a Convolutional Neural Network (CNN) or Foureir Neuro Operators (FNO), will be trained to distinguish these two types of BP radiators in both synthetic and real BP images. Additionally, DL methods will investigate the potential for automatically grouping BP radiators into clusters that correspond to rupture segments influenced by abrupt fault kinematics changes, such as jumps in rupture speed, slip variation, and alterations in sub-fault geometry. This automatic segmentation process bears similarities to traditional image segmentation and recognition tasks, solvable through encoder-decoder CNN architectures like U-Net (Ronneberger, 2015). One could also aim to explore whether DL methods can directly estimate rupture kinematic parameters (e.g., slip, rupture length, and speed).

However, the methodology requires further refinement to accurately model complex scatterings and coherence patterns, particularly for source-side incoherency, where direct measurement of coherence patterns is often hampered by the scarcity of EGF observations around the fault zone. Earthquake swarms and repeating earthquakes offer a natural laboratory for observing source-side scatterings, enabling the study of cross-correlation among small earthquakes to derive coherence patterns and correlation lengths, for instance, in the Japan subduction zone (Ide, 2019). Such observations could inform adjustments to the parameters of the multi-plane-wave simulator. Additionally, modeling incoming scattered waves demands consideration not only of azimuthal variation but also of changes in amplitude and polarity. Incorporating more control parameters could enhance the simulation of P-coda waves, while fitting CC patterns necessitates not just phase information—commonly used in BPs—but also matching the amplitude decay pattern for a more comprehensive analysis.

6 Conclusion

In this study, we developed an advanced stochastic waveform generator based on the superposition of plane waves, designed to replicate the incoherency observed in GFs for teleseismic array recordings. This generator employs ray theory to calculate travel times and aggregates random plane waves to mimic the complex high-frequency waveform intricacies resulting from local/path scatterings and velocity heterogeneities. Through a grid-search process, we optimized the IGFs to closely match the observed decay patterns in waveform coherence over time and across interstation distances.

Armed with these realistically IGFs, we discovered that incoherency not only introduces artifacts into BPs but also significantly enhances BP's imaging capabilities. Specifically, it facilitates the detailed imaging of the central segments of homogeneous ruptures and aids in distinguishing between closely situated sub-sources. Our examination of shadowing and tailing artifacts further illustrates that rupture speeds can be reliably inferred by analyzing

leading BP radiators, with the systematic error in rupture speed estimation quantifiably assessed through this approach.

Looking ahead, we intend to conduct a series of synthetic tests, engaging in comprehensive forward-modeling exercises and establishing benchmarks for BP imaging. Our ultimate goal is to create a versatile platform that will serve as a foundation for future BP synthetic tests, pushing the boundaries of earthquake source analysis and contributing to a deeper understanding of earthquake rupture dynamics. This work underscores the critical role of incorporating waveform incoherency in seismic modeling and highlights the potential of innovative methods to advance the field of earthquake seismology.

Acknowledgements

All authors are supported by the NSF CAREER grant (EAR-1848486) and the Leon and Joanne V.C.Knopoff Fund. Figures were produced using Generic Mapping Tools (GMT) and MATLAB. The Python software package ObSpy was used for data requests.

Open Research

All seismic data are downloaded through the IRIS Wilber 3 system (https://ds.iris.edu/wilber3/) and the TA (Transportable Array; IRIS, 2003) seismic network. The MATLAB code of MUSIC BP is available at https://github.com/lsmeng/MUSICBP. Codes for generating incoherent Green's Functions and for synthetic tests will be available at the time of publication.

References

Bao, H., Xu, L., Meng, L., Ampuero, J.-P., Gao, L., & Zhang, H. (2022). Global frequency of oceanic and continental supershear earthquakes. Nature Geoscience, 15, 942–949. https://doi.org/10.1038/s41561-022-01055-5

Berteussen, K. A., Christoffersson, A., Husebye, E. S., & Dahle, A. (1975). Wave scattering theory in analysis of P-wave anomalies at NORSAR and LASA. Geophysical Journal International, 42(2), 403-417, https://doi.org/10.1111/j.1365-246X.1975.tb05869.x

Bruhat, L., Fang, Z., & Dunham, E. M. (2016). Rupture complexity and the supershear transition on rough faults. Journal of Geophysical Research: Solid Earth, 121(1), 210-224, https://doi.org/10.1002/2015JB012512

Capon, J., & Berteussen, K. A. (1974). A random medium analysis of crust and upper mantle structure under NORSAR. Geophysical Research Letters, 1(7), 327-328, https://doi.org/10.1029/GL001i007p00327

Dunham, E. M., Kozdon, J. E., Belanger, D., & Cong, L. (2011). Earthquake ruptures on rough faults. In Multiscale and Multiphysics Processes in Geomechanics (pp. 145-148). Springer, Berlin, Heidelberg. https://doi.org/10.1007/978-3-642-19630-0_37

Emoto, K., & Sato, H. (2018). Statistical characteristics of scattered waves in three-dimensional random media: comparison of the finite difference simulation and statistical methods. Geophysical Journal International, 215(1), 585-599, https://doi.org/10.1093/gji/ggy298

Fan, W., & Shearer, P. M. (2015). Detailed rupture imaging of the 25 April 2015 Nepal earthquake using teleseismic P waves. Geophysical Research Letters, 42(14), 5744-5752, https://doi.org/10.1002/2015GL064587

Fan, W., & Shearer, P. M. (2016). Local near instantaneously dynamically triggered aftershocks of large earthquakes. Science, 353(6304), 1133–1136, https://doi.org/10.1126/science.aag0013

Fletcher, J. B., Spudich, P., & Baker, L. M. (2006). Rupture propagation of the 2004 Parkfield, California, earthquake from observations at the UPSAR. Bulletin of the Seismological Society of America, 96(4B), S129-S142, https://doi.org/10.1785/0120050812

Fukahata, Y., Yagi, Y., & Rivera, L. (2014). Theoretical relationship between back-projection imaging and classical linear inverse solutions. Geophysical Journal International, 196(1), 552-559, https://doi.org/10.1093/gji/ggt392

Hayes, G. & Ji, C. (2009).Preliminary Result of the May 28, 2009 Mw 7.3 Earthquake Offshore Honduras,http://earthquake.usgs.gov/earthquakes/eqinthenews/2009/us2009heak/finite_fault.php,last accessed August 29, 2013.

Hayes, G. P. (2017). The finite, kinematic rupture properties of great-sized earthquakes since 1990. Earth and Planetary Science Letters, 468, 94–100. https://doi.org/10.1016/j.epsl.2017.04.003

Hicks, S.P., Okuwaki, R., Steinberg, A., Rychert, C.A., Harmon, N., Abercrombie, R.E., Bogiatzis, P., Schlaphorst, D., Zahradnik, J., Kendall, J.M. and Yagi, Y., 2020. Back-propagating supershear rupture in the 2016 M w 7.1 Romanche transform fault earthquake. *Nature Geoscience*, *13*(9), pp.647-653.

Huang, Y., Ampuero, J. P., & Helmberger, D. V. (2016). The potential for supershear earthquakes in damaged fault zones–theory and observations. Earth and Planetary Science Letters, 433, 109-115, https://doi.org/10.1016/j.epsl.2015.10.046.

Ide, S. (2019). Detection of low-frequency earthquakes in broadband random time sequences: Are they independent events?. Journal of Geophysical Research: Solid Earth, 124, 8166–8625e. https://doi.org/10.1029/2019JB017643

IRIS Transportable Array. (2003). USArray Transportable Array. International Federation of Digital Seismograph Networks. https://doi.org/10.7914/SN/TA

Kehoe, H., Kiser, E., & Okubo, P. (2018, December). The rupture process of the 2018 M w 6.9 Hawaíi earthquake as revealed by a genetic algorithm-based source imaging technique. In AGU Fall Meeting Abstracts (Vol. 2018, pp. V31C-06).

Kiser, E., & M. Ishii (2011), The 2010 Mw 8.8 Chile earthquake: Triggering on multiple segments and frequency-dependent rupture behavior, Geophysical Research Letters, 38, L07301, https://doi.org/10.1029/2011GL047140.

Kiser, E., & Ishii, M. (2017). Back-projection imaging of earthquakes. Annual Review of Earth and Planetary Sciences, 45(1), 271–299. https://doi.org/10.1146/annurev-earth-063016-015801

Kostrov, B. V. (1964). Selfsimilar problems of propagation of shear cracks. Journal of Applied Mathematics and Mechanics, 28(5), 1077–1087, https://doi.org/10.1016/0021-8928(64)90010-3

Lay, T., Kanamori, H., Ammon, C. J., Koper, K. D., Hutko, A. R., Ye, L., & Rushing, T. M. (2012). Depth-varying rupture properties of subduction zone megathrust faults. Journal of Geophysical Research: Solid Earth, 117(B4). https://doi.org/10.1029/2011JB009133

Li, B., Wu, B., Bao, H., Oglesby, D. D., Ghosh, A., Gabriel, A.-A., et al. (2022). Rupture heterogeneity and directivity effects in back-projection analysis. Journal of Geophysical Research: Solid Earth, 127(3), e2021JB022663. https://doi.org/10.1029/2021JB022663

Li, J., Kim, T., Lapusta, N., Biondi, E. and Zhan, Z., 2023. The break of earthquake asperities imaged by distributed acoustic sensing. *Nature*, *620*(7975), pp.800-806.

Mai, P. M., Schorlemmer, D., Page, M., Ampuero, J. P., Asano, K., Causse, M., & Zielke, O. (2016).

693 The earthquake-source inversion validation (SIV) project. Seismological Research Letters, 87(3),
694 690-708, https://doi.org/10.1785/0220150231

695 Mai, P. M., Galis, M., Thingbaijam, K. K. S., Vyas, J. C., & Dunham, E. M. (2017, December).
696 Rupture Dynamics and Seismic Radiation on Rough Faults for Simulation-Based PSHA. In 2017 Fall
697 Meeting.

698 Melgar, D., & Hayes, G. P. (2017). Systematic observations of the slip pulse properties of large
699 earthquake ruptures. Geophysical Research Letters, 44, 9691–9698.
700 https://doi.org/10.1002/2017GL074916

701 Meng, L., Inbal, A. and Ampuero, J.P., (2011). A window into the complexity of the dynamic rupture
702 of the 2011 Mw 9 Tohoku-Oki earthquake. Geophysical Research Letters, 38(7).

703 Meng. L., Ampuero, J.-P., Stock, J., Duputel, Z., Luo, Y., & Tsai, V. C. (2012a). Earthquake in a maze:
704 compressional rupture branching during the 2012 Mw 8.6 Sumatra earthquake, Science, 337(6095),
705 724-726. https://doi.org/10.1126/science.1224030.

706 Meng, L., Ampuero, J. P., Luo, Y., Wu, W., & Ni, S. (2012b). Mitigating artifacts in back-projection
707 source imaging with implications for frequency-dependent properties of the Tohoku-Oki earthquake.
708 Earth, planets and space, 64(12), 1101-1109, https://doi.org/10.5047/eps.2012.05.010

709 Meng, L., Allen, R. M., & Ampuero, J. -P. (2014). Application of Seismic Array Processing to
710 Earthquake Early Warning. Bulletin of the Seismological Society of America, 104(5), 2553–2561.
711 https://doi.org/10.1785/0120130277

712 Meng, L., Bao, H., Huang, H., Zhang, A., Bloore, A., & Liu, Z. (2018). Double pincer movement:
713 Encircling rupture splitting during the 2015 Mw 8.3 Illapel earthquake. Earth and Planetary Science
714 Letters, 495, 164–173. https://doi.org/10.1016/j.epsl.2018.04.057

715 Nielsen, S., & Madariaga, R. (2003). On the self-healing fracture mode. Bulletin of the Seismological
716 Society of America, 93(6), 2375-2388. https://doi.org/10.1785/0120020090

717 Ohnaka, M., & Yamashita, T. (1989), A cohesive zone model for dynamic shear faulting based on
718 experimentally inferred constitutive relation and strong motion source parameters, J. Geophys. Res.,
719 94(B4), 4089–4104, https://doi.org/10.1029/JB094iB04p04089.

720 Okuwaki, R., & Yagi, Y. (2018). Role of geometric barriers in irregular-rupture evolution during the
721 2008 Wenchuan earthquake. Geophysical Journal International, 212(3), 1657-1664.
722 https://doi.org/10.1093/gji/ggx502

723 Okuwaki, R., Kasahara, A., Yagi, Y., Hirano, S., & Fukahata, Y. (2019). Backprojection to image slip.
724 Geophysical Journal International, 216(3), 1529-1537, https://doi.org/10.1093/gji/ggy505

725 Ronneberger, O., Fischer, P., & Brox, T. (2015). U-net: Convolutional networks for biomedical image
726 segmentation. In International Conference on Medical image computing and computer-assisted
727 intervention. Springer, Cham, 234-241, https://doi.org/10.1007/978-3-319-24574-4_28

728 Rost, S., & Thomas, C. (2002). Array seismology: Methods and applications. Reviews of Geophysics,
729 40(3), 2-1-2–27. https://doi.org/10.1029/2000RG000100

730 Tinti, E., Fukuyama, E., Piatanesi, A., & Cocco, M. (2005). A kinematic source-time function
731 compatible with earthquake dynamics. Bulletin of the Seismological Society of America, 95(4),
732 1211–1223. https://doi.org/10.1785/0120040177

733 Uchide, T., Yao, H., & Shearer, P. M. (2013). Spatio-temporal distribution of fault slip and
734 high-frequency radiation of the 2010 El Mayor-Cucapah, Mexico earthquake. Journal of Geophysical
735 Research: Solid Earth, 118(4), 1546-1555, https://doi.org/10.1002/jgrb.50144

Vallée, M., and C. Satriano (2014), Ten year recurrence time between two major earthquakes affecting the same fault segment, Geophysical Research Letters, 41, 2312–2318, https://doi.org/10.1002/2014GL059465.

van den Ende, M., & Ampuero, J. P. (2021). Evaluating seismic beamforming capabilities of distributed acoustic sensing arrays. Solid Earth, 12(4), 915-934, https://doi.org/10.5194/se-12-915-2021

Xie, Y. & Meng, L. (2020). A multi-array back-projection approach for tsunami warning. Geophysical Research Letters, 47, e2019GL085763. https://doi.org/10.1029/2019GL085763

Xie, Y., Bao, H., & Meng, L. (2021). Source imaging with a multi-array local back-projection and its application on the 2019 Mw 6.4 and Mw 7.1 Ridgecrest earthquakes. Journal of Geophysical Research: Solid Earth, 126, e2020JB021396. https://doi.org/10.1029/2020JB021396

Yagi, Y., Nakao, A., & Kasahara, A. (2012). Smooth and rapid slip near the Japan Trench during the 2011 Tohoku-oki earthquake revealed by a hybrid back-projection method. Earth and Planetary Science Letters, 355, 94-101, https://doi.org/10.1016/j.epsl.2012.08.018

Yao, H., Gerstoft, P., Shearer, P. M., & Mecklenbräuker, C. (2011). Compressive sensing of the Tohoku-Oki Mw 9.0 earthquake: Frequency-dependent rupture modes. Geophysical Research Letters, 38, L20310, https://doi.org/10.1029/2011GL049223

Yao, H., Shearer, P. M., & Gerstoft, P. (2013). Compressive sensing of frequency-dependent seismic radiation from subduction zone megathrust ruptures. Proceedings of the National Academy of Sciences, 110(12), 4512–4517. https://doi.org/10.1073/pnas.1212790110

Ye, L., Lay, T., Kanamori, H., & Rivera, L. (2016). Rupture characteristics of major and great (Mw≥ 7.0) megathrust earthquakes from 1990 to 2015: 1. Source parameter scaling relationships. Journal of Geophysical Research: Solid Earth, 121(2), 826-844, https://doi.org/10.1002/2015JB012426

Yin, J., & Yao, H. (2016). Rupture and frequency-dependent seismic radiation of the 2012 M w 8.6 Sumatra strike-slip earthquake. Geophysical Journal International, 205(3), 1682-1693, https://doi.org/10.1093/gji/ggw105

Yin, J., & Denolle, M. A. (2019). Relating teleseismic backprojection images to earthquake kinematics. Geophysical Journal International, 217(2), 729–747. https://doi.org/10.1093/gji/ggz048

Yoffe, E. H. (1951). LXXV. The moving Griffith crack. The London, Edinburgh and Dublin Philosophical Magazine and Journal of Science, 42(330), 739–750. https://doi.org/10.1080/14786445108561302

Zeng, H., Wei, S., & Wu, W. (2020). Sources of uncertainties and artefacts in back-projection results. Geophysical Journal International, 220(2), 876-891. https://doi.org/10.1093/gji/ggz482

Figure1.

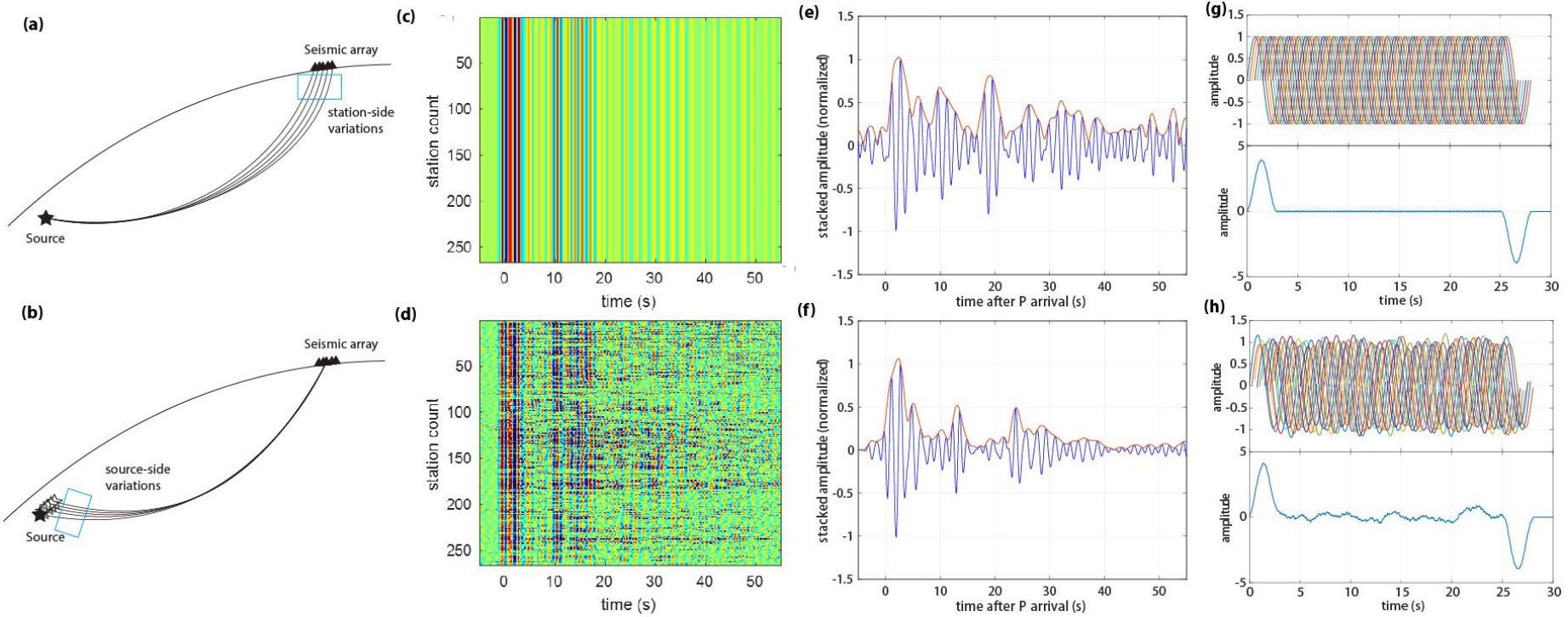
(a)
Seismic array
station-side
variations
Source
(b)
Seismic array
source-side
variations
Source
(c)
station count
time (s)
(d)
station count
time (s)
(e)
stacked amplitude (normalized)
time after P arrival (s)
(f)
stacked amplitude (normalized)
time after P arrival (s)
(g)
amplitude
amplitude
time (s)
(h)
amplitude
amplitude
time (s)

Figure2.

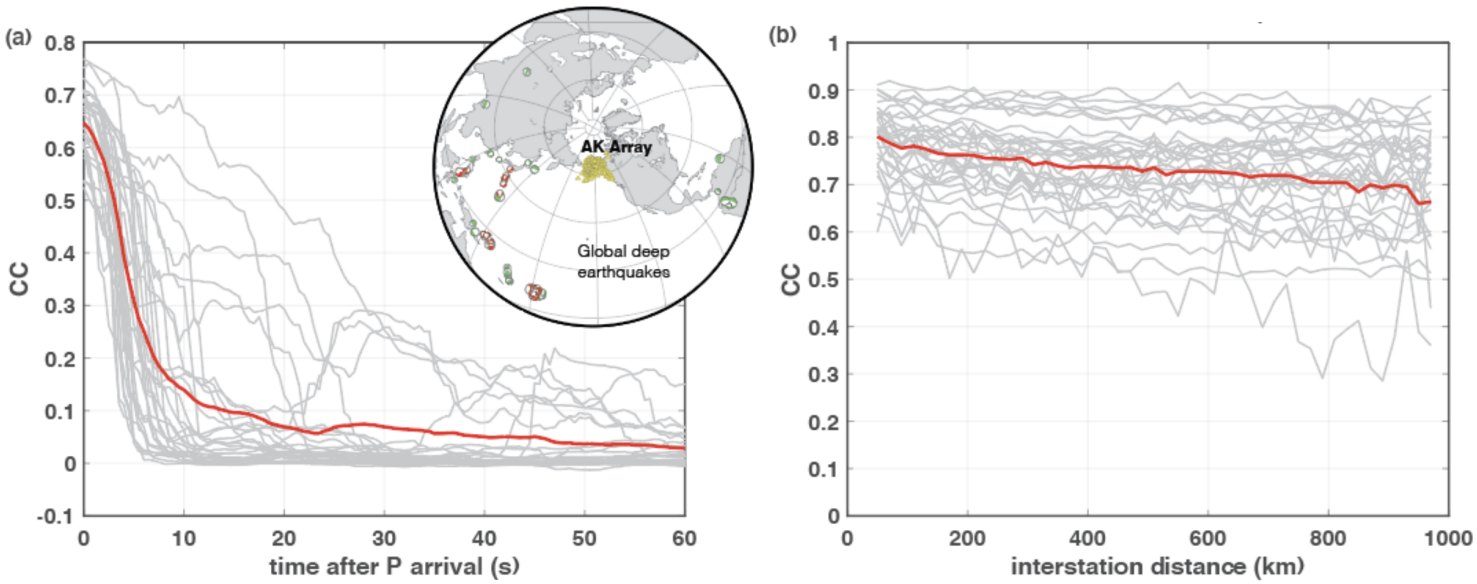
(a)
CC
time after P arrival (s)
AK Array
Global deep
earthquakes
(b)
CC
interstation distance (km)

Figure3.

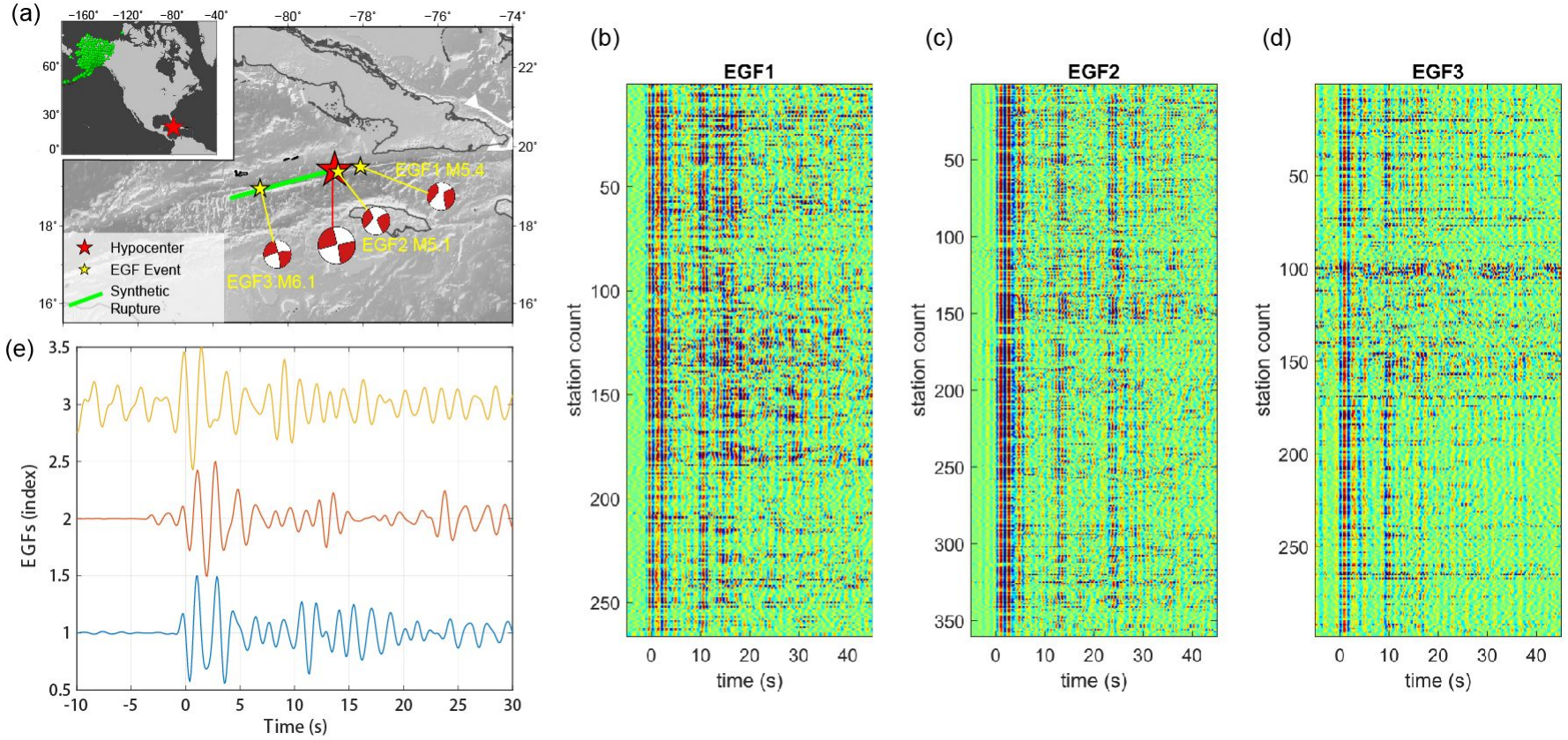
(a)
−160° −120° −80° −40°
−80° −78° −76° −74°
60°
30°
0°
22°
20°
18°
16°
EGF1 M5.4
EGF2 M5.1
EGF3 M6.1
Hypocenter
EGF Event
Synthetic Rupture
(b)
EGF1
(c)
EGF2
(d)
EGF3
station count
time (s)
(e)
EGFs (index)
Time (s)

Figure4.

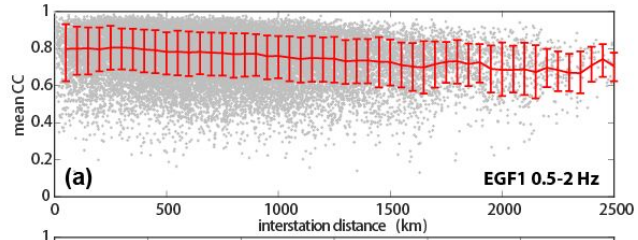
(a)
EGF1 0.5-2 Hz
mean CC
interstation distance (km)

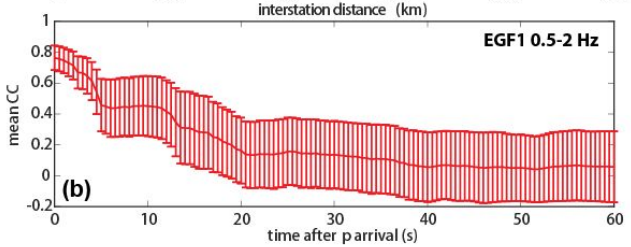
(b)
EGF1 0.5-2 Hz
mean CC
time after p arrival (s)

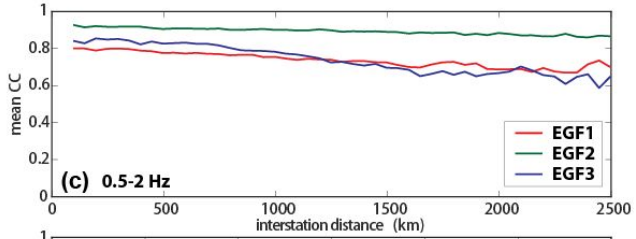
(c) 0.5-2 Hz
EGF1
EGF2
EGF3
mean CC
interstation distance (km)

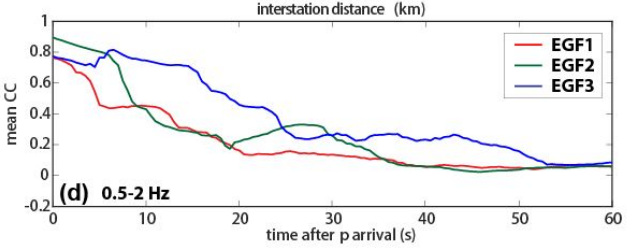
(d) 0.5-2 Hz
EGF1
EGF2
EGF3
mean CC
time after p arrival (s)

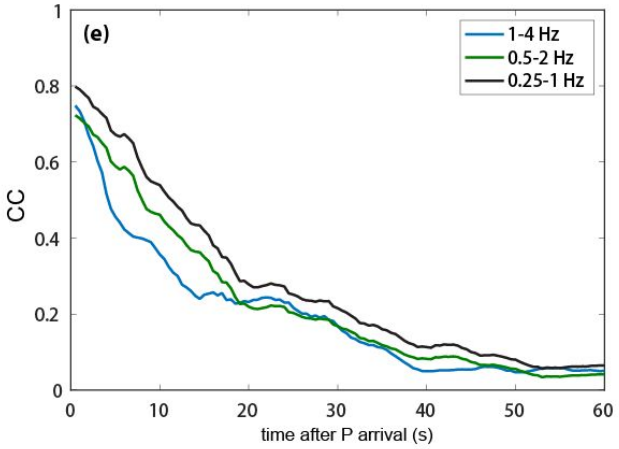
(e)
1-4 Hz
0.5-2 Hz
0.25-1 Hz
CC
time after P arrival (s)

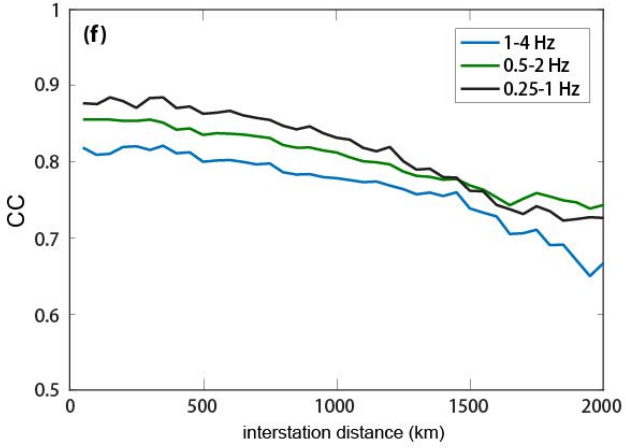
(f)
1-4 Hz
0.5-2 Hz
0.25-1 Hz
CC
interstation distance (km)

Figure5.

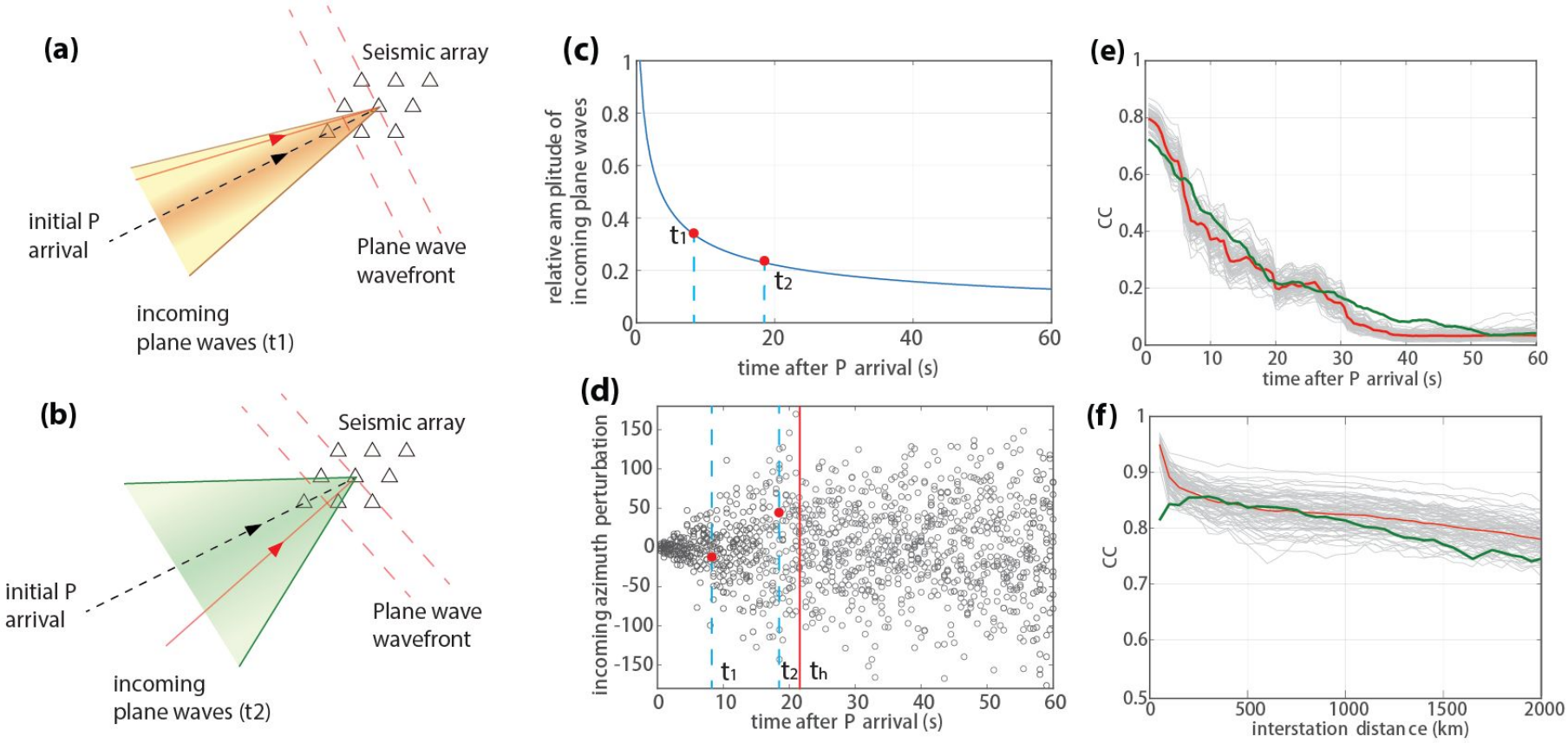
(a)
Seismic array
initial P arrival
Plane wave wavefront
incoming plane waves (t1)
(b)
Seismic array
initial P arrival
Plane wave wavefront
incoming plane waves (t2)
(c)
relative am plitude of incoming plane waves
t1
t2
time after P arrival (s)
(d)
incoming azimuth perturbation
t1
t2
th
time after P arrival (s)
(e)
CC
time after P arrival (s)
(f)
CC
interstation distan ce (km)

Figure6.

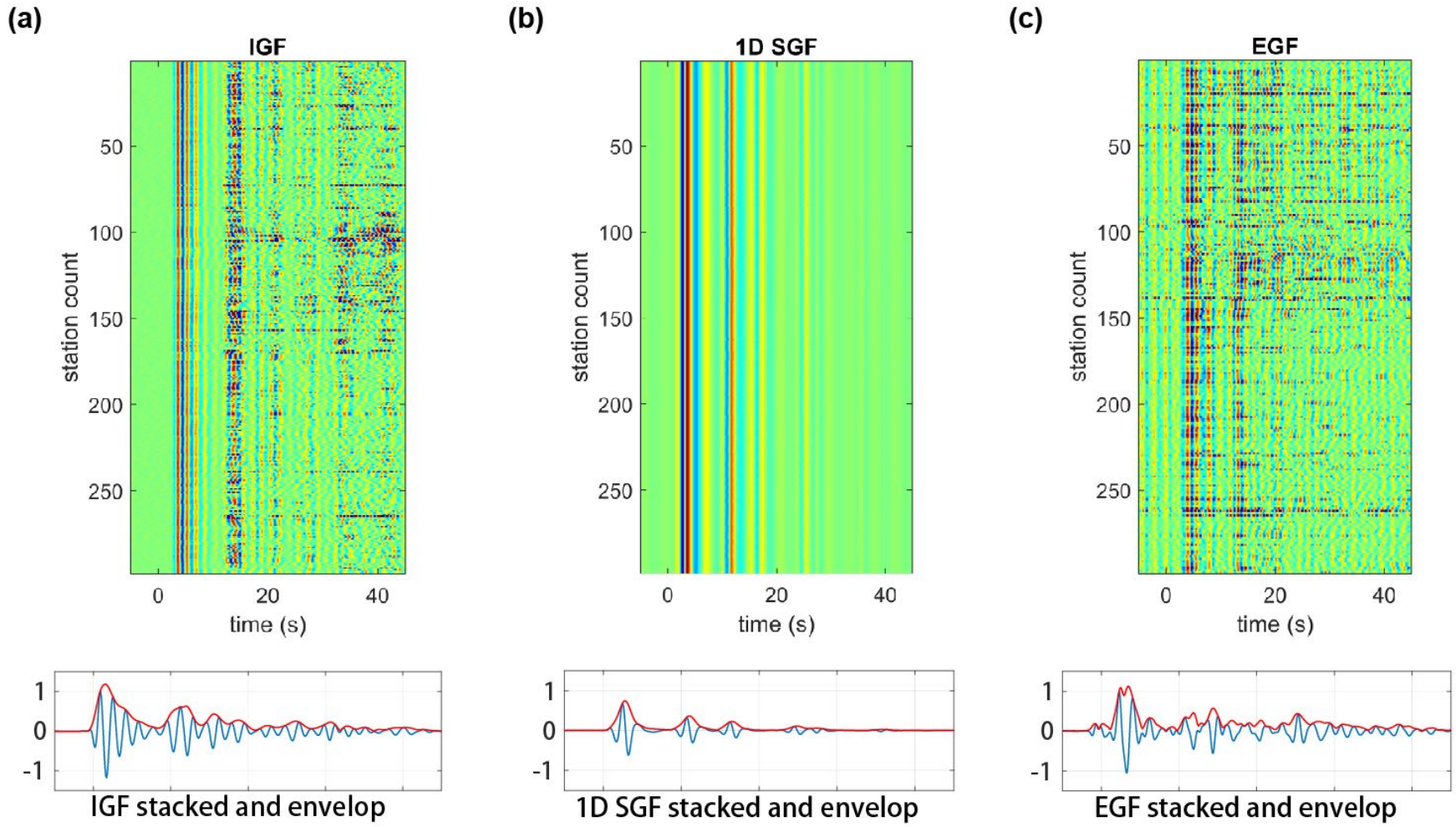
(a)
IGF
station count
time (s)
IGF stacked and envelop
(b)
1D SGF
station count
time (s)
1D SGF stacked and envelop
(c)
EGF
station count
time (s)
EGF stacked and envelop

Figure7.

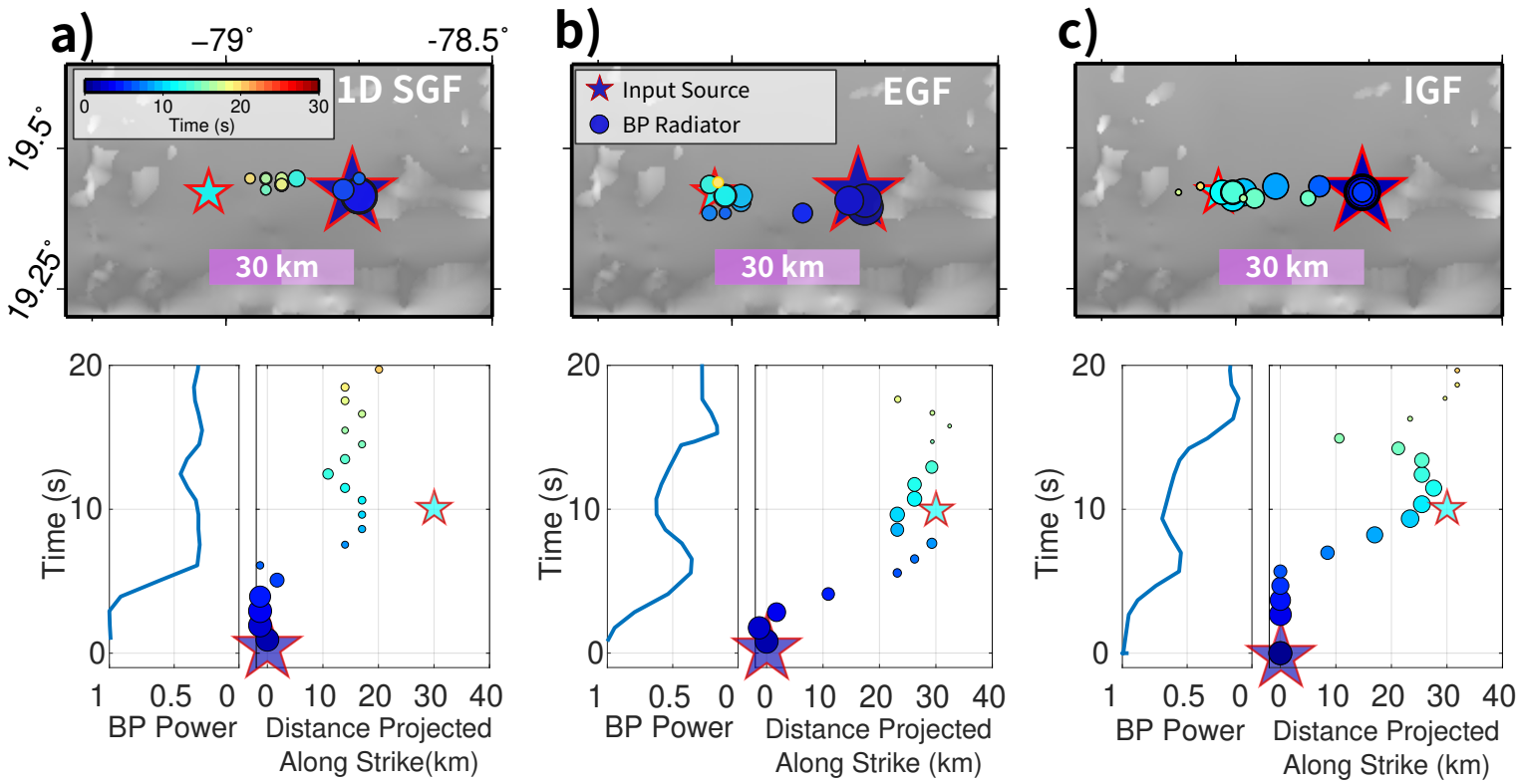
a)
−79˚
-78.5˚
19.5˚
19.25˚
0
10
20
30
Time (s)
1D SGF
30 km
b)
Input Source
BP Radiator
EGF
30 km
c)
IGF
30 km
Time (s)
BP Power
Distance Projected
Along Strike(km)
Along Strike (km)

Figure8.

Conceptual Paradigm of the Starting/Stopping Phase

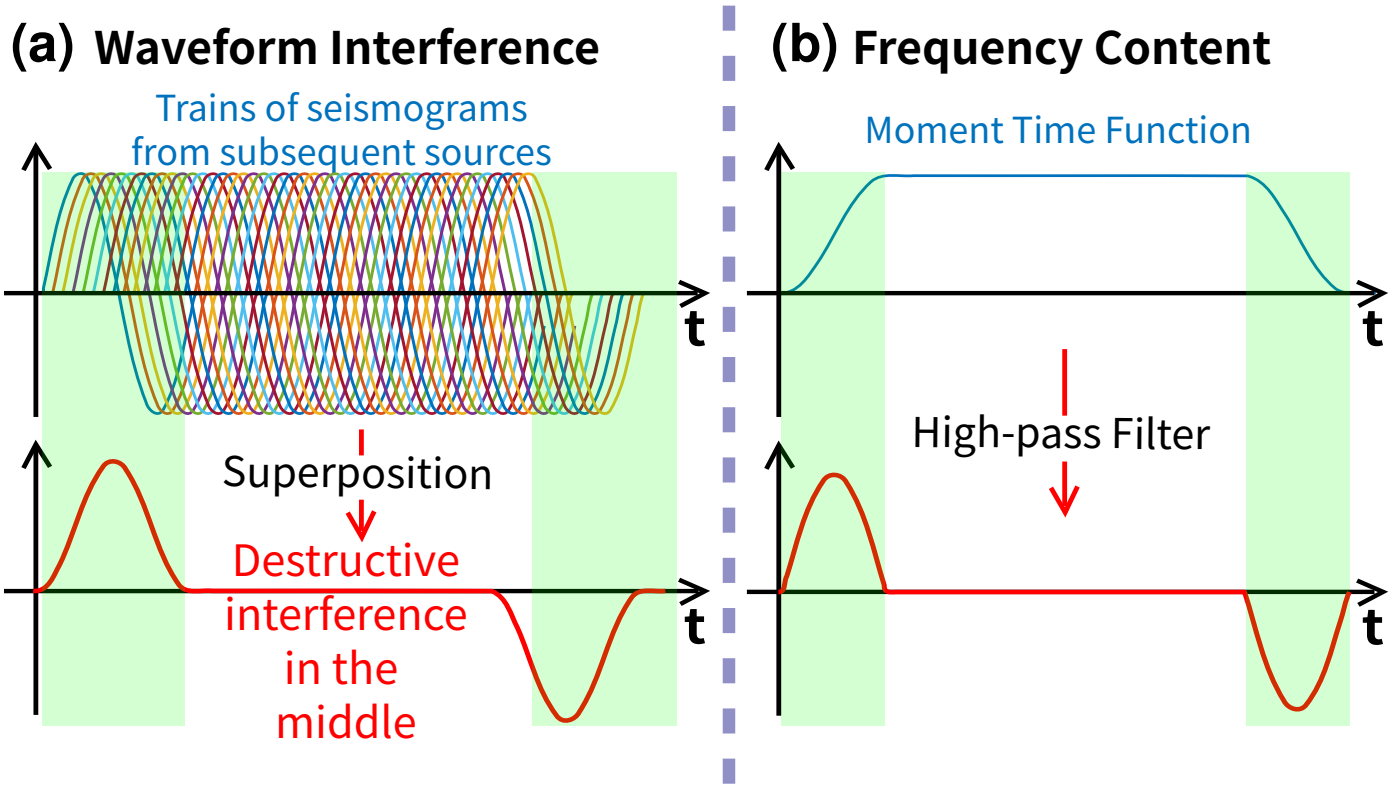

Figure9.

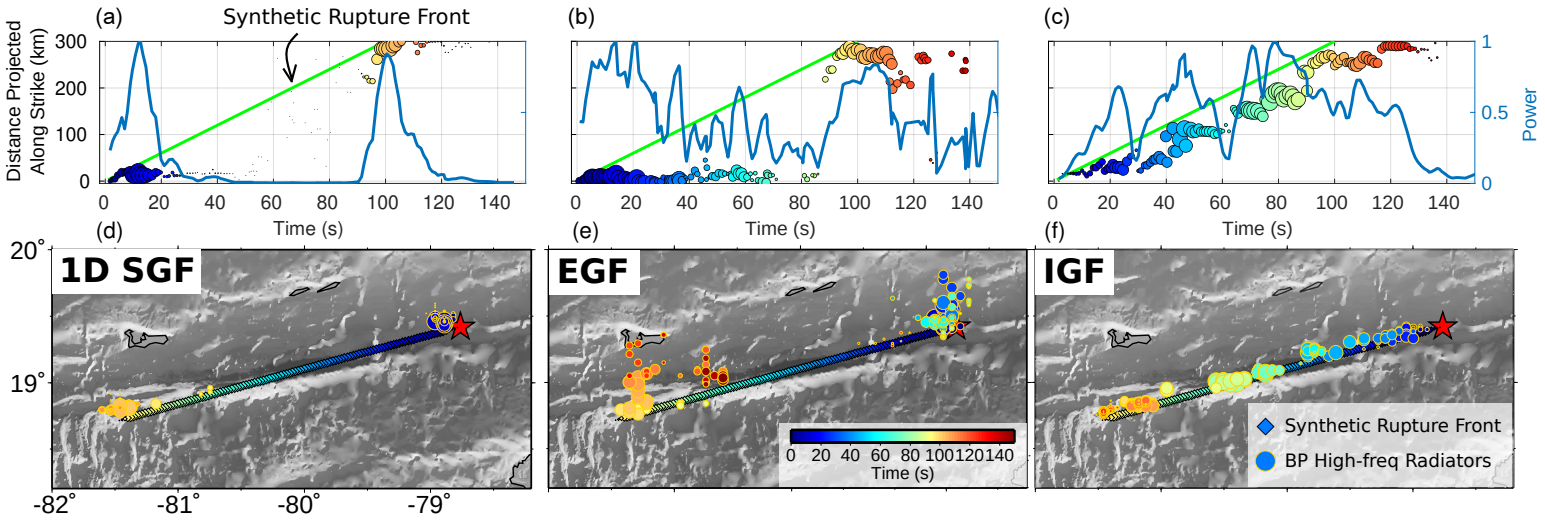
(a)
Synthetic Rupture Front
Distance Projected Along Strike (km)
300
200
100
0
0 20 40 60 80 100 120 140
Time (s)
(b)
0 20 40 60 80 100 120 140
Time (s)
(c)
1
0.5
0
Power
0 20 40 60 80 100 120 140
Time (s)
(d)
1D SGF
(e)
EGF
0 20 40 60 80 100120140
Time (s)
(f)
IGF
Synthetic Rupture Front
BP High-freq Radiators
20°
19°
-82°
-81°
-80°
-79°

Figure10.

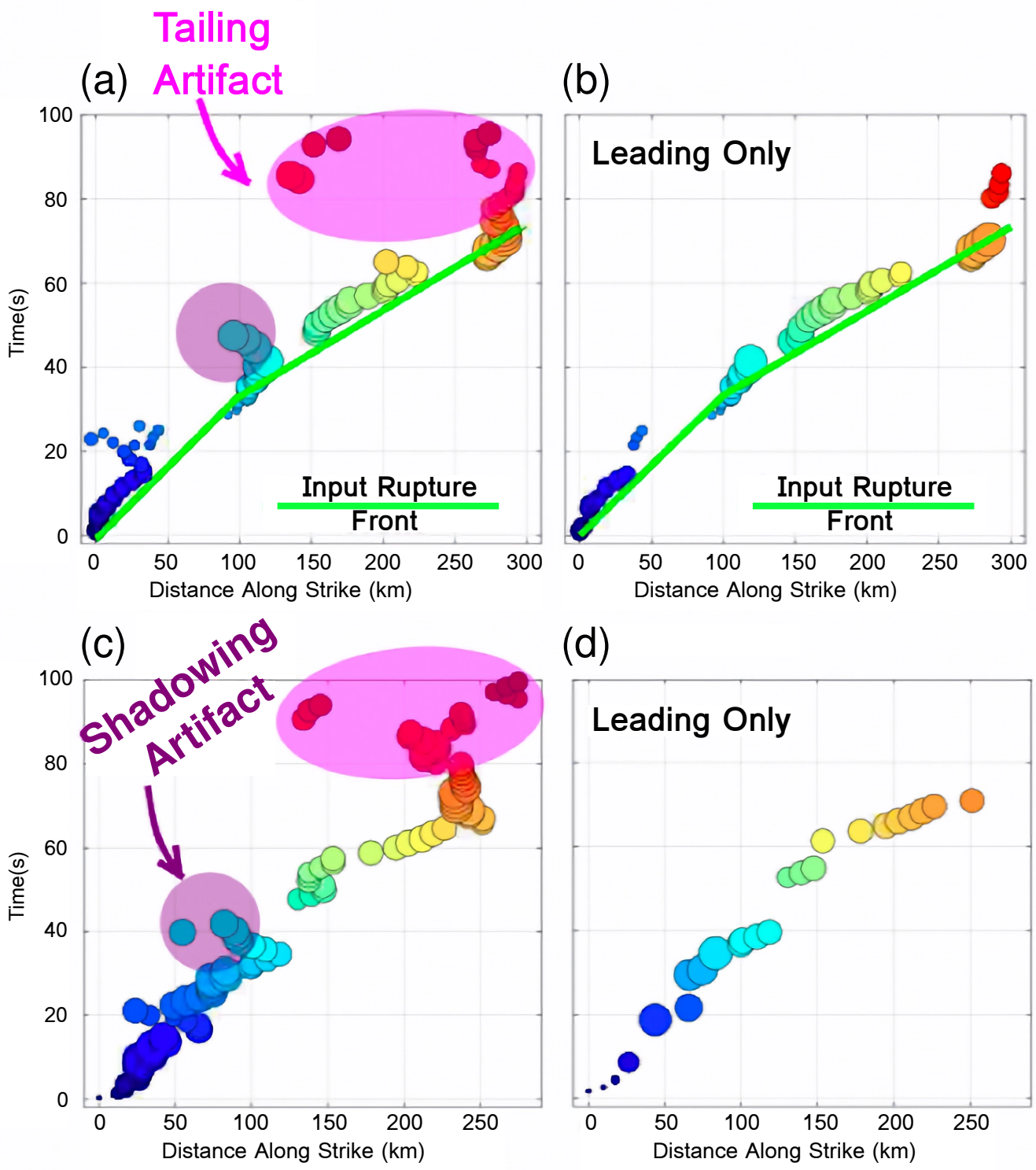
(a)
Tailing Artifact
Input Rupture Front
Time(s)
Distance Along Strike (km)
(b)
Leading Only
Input Rupture Front
Distance Along Strike (km)
(c)
Shadowing Artifact
Time(s)
Distance Along Strike (km)
(d)
Leading Only
Distance Along Strike (km)